Table I. Demographic and clinical data for each group of patients

Variable[a]	*Control veins*	C_{2-3}	C_{4-5}
Limbs	10	27	23
Sex			
Men	9	5	4
Women	1	17	12
Age, years	65.9 ± 11.4	62.8 ± 13.8	64.7 ± 15.1
Disease duration, years	. . .	13.4 ± 11.7	17.8 ± 16.9
Cholesterol, mg/dL			
Total	191.3 ± 43.3	186.7 ± 41.9	182.2 ± 45.2
LDL	121.3 ± 22.7	116.6 ± 31.6	117.5 ± 34.2
HDL	39.2 ± 15.2	43.1 ± 12.8	41.0 ± 12.3
Triglyceride, mg/dL	108.3 ± 51.2	113.1 ± 24.1	112.5 ± 32.2
Hemoglobin A_{1C}, %	6.0 ± 1.9	5.9 ± 1.2	5.8 ± 2.5

HDL, High-density lipoprotein; *LDL*, low-density lipoprotein.
Categoric data are expressed as number and continuous data as mean ± standard deviation.

distribution of lipid molecules in incompetent GSVs in VV patients.

METHODS

All procedures used in this study were approved by the Ethics Committee of Clinical Research of the Hamamatsu University School of Medicine.

Sample collection. We enrolled 48 patients in this study between April 2008 and December 2010. We obtained GSV tissue from of 38 VV patients (50 limbs) who underwent GSV stripping. Clinical information is summarized in Table I. By CEAP clinical severity scores,[7] 16 samples were assigned to C_2 (simple VV), 11 to C_3 (VV with ankle swelling), 21 to C_4 (VV with skin changes), and 2 to C_5 (VV with healed ulcer). To investigate the association between the tissue lipid profiles and disease severity, we classified the VV patients into two groups: C_{2-3} (moderate VV group) and C_{4-5} (severe VV group). As control veins (CV), segmental GSV tissues were harvested from 10 patients (10 limbs) with peripheral artery occlusive disease who underwent infrainguinal bypass with reversed GSV grafting (Table I).

To maintain tissue morphology and minimize molecular degradation, tissue samples were immediately frozen in liquid nitrogen and stored at −80°C until matrix-assisted laser desorption–ionization IMS (MALDI-IMS) analysis; other samples were preserved in 10% formalin for histopathologic examination.

All patients underwent duplex ultrasound scans with a 7.5-MHz transducer (LOGIC 500; GE Yokogawa Medical, Tokyo, Japan) to assess venous hemodynamics. Clinical disease severity was graded using the standard CEAP classification according to the recommendations of an International Consensus Committee on Chronic Venous Disease.[7] Venodynamic studies were performed using duplex scanning, with patients scanned while standing to assess reflux throughout the GSV. Reflux was defined as flow in the reverse direction of the physiologic flow of duration >0.5 seconds after a provocation maneuver.[8] All VV patients had retrograde flow in the saphenofemoral junction; the control patients had no reflux in the GSV. We analyzed the GSV tissue that was in close to the saphenofemoral junction, excluding the terminal valve.

Imaging mass spectrometry. We cut the frozen tissues into 8-μm-thick longitudinal sections using a cryostat (CM1950; Leica, Wetzler, Germany). Sections were thaw-mounted onto indium tin oxide–coated glass slides (Bruker Daltonics, Bremen, Germany) and dried at room temperature. A total of 500 μL of 2,5-dihydroxybenzoic acid solution (50 mg/mL in methanol/water, 7:3 [v/v]) was sprayed on the sample sections using a 0.2-mm nozzle airbrush (Procon Boy FWA Platinum; Mr. Hobby, Tokyo, Japan). A 15-cm distance was maintained between the nozzle and the tissue surface during spraying.

We performed IMS using a MALDI time of flight (TOF)/TOF-type instrument (Ultraflex II TOF/TOF; Bruker Daltonics, Bremen, Germany) equipped with a 355-nm neodymium-doped yttrium aluminium garnet laser (repetition rate, 200 Hz). Data were acquired with a step size of 50 μm for the samples in the positive ion mode (reflector mode). The mass spectrometer parameters were set to obtain the highest sensitivity with mass/charge ratio (*m/z*) values of 400 to 1000. All spectra were acquired automatically using Flex Imaging software (Bruker Daltonics). The laser was used to irradiate each position 100 times. The peaks were normalized to the total ion current and then compared. Ion images were created using Flex Imaging software (Bruker Daltonics).

Tandem MS. Tandem MS (MS/MS) was performed on tissue sections using a linear quadruple ion trap LTQ-XL mass spectrometer (Thermo Fisher Scientific, Waltham Mass), as described previously.[9] Precursor and fragment ions obtained by collision-induced dissociation were ejected from the ion trap and analyzed. Collision energy was set to 30% (this unit is customized for LTQ-XL; 100% indicates the energy that completely fragments the peptide Met-Arg-Phe-Ala). The laser energy was set to 30 μJ. Specific fragment patterns of triglycerides (TGs), LPC, and PC were confirmed using previous reports.[1,3,10-12]

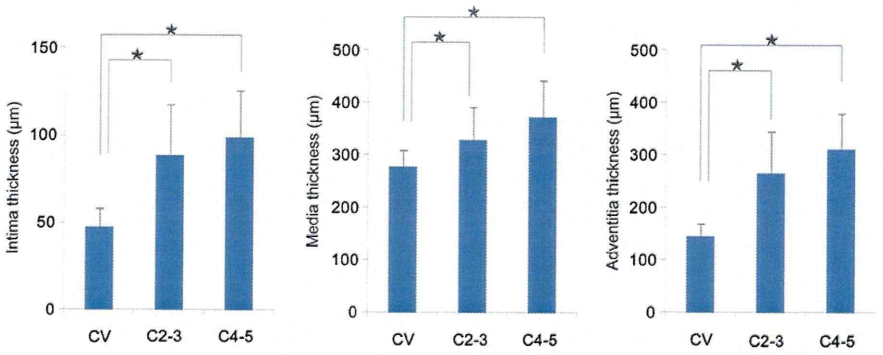

Fig 1. Thickness of the great saphenous vein wall. The measured thickness of the **(left)** intima, **(middle)** media, and **(right)** adventitia layers is compared among the control vein (*CV*) and varicose veins from the CEAP $C_{2\text{-}3}$ and $C_{4\text{-}5}$ groups. $^*P < .05$ indicates a statistically significant difference. The *error bars* show the standard deviation.

Histopathologic examinations. Specimens for light microscopy were fixed in 10% neutral-buffered formalin solution and were processed to prepare 4-mm-thick paraffin sections. Sections were stained with hematoxylin and eosin (HE) and elastica van Gieson (EVG). A light microscope was used for quantitative measurements.

Biochemical quantitation. Total lipids were extracted from homogenized tissue as described previously.[13] Phospholipids and TGs were quantified using colorimetric methods (Wako, Osaka, Japan).

Immunostaining. Tissue sections (8 μm) were fixed with 4% paraformaldehyde in phosphate-buffered saline (pH 7.4) for 10 minutes at room temperature. Sections were rinsed with phosphate-buffered saline, preincubated with 10% normal goat serum (Nichirei Biosciences, Tokyo, Japan), and incubated overnight at 4°C with rabbit anti-von Willebrand factor (1:400; Acris Antibodies GmbH, Herford, Germany) and mouse anti-D2-40 (1:200; Acris Antibodies GmbH, Herford, Germany). Immunoreactivity was visualized using Alexa Fluor 488-conjugated antirabbit immunoglobulin G and Alexa Fluor 594-conjugated anti-mouse immunoglobulin G (Molecular Probes; Invitrogen, Carlsbad, Calif). All Alexa Fluor-conjugated secondary antibodies were diluted 200-fold for use. The slides were mounted in a glycerol-based Vectashield medium (Vector Laboratories, Burlingame, Calif) containing the nucleus staining reagent 4′,6-diamidino-2-phenylindole.

Statistical analysis. Results have been summarized using descriptive statistics. All data are expressed as mean ± standard deviation. The significance of the differences between groups with respect to vein wall thickness, lipid content, ratio of intensity, and the number of lymphatic vessels was determined by one-way analysis of variance, followed by the Tukey test. A value of $P < .05$ was considered significant. All statistical analyses were performed with StatView 5.0 software (SAS Institute, Tokyo, Japan).

RESULTS

Clinical information. Patient demographics are reported in Table I. The control and $C_{2\text{-}3}$, and $C_{4\text{-}5}$ VV groups did not differ significantly in age, disease duration, serum total cholesterol, serum low-density lipoprotein (LDL), serum high-density lipoprotein (HDL), serum TG contents, and hemoglobin A_{1C}. The only significant difference between groups was the sex ratio.

Histopathologic examinations. The intimal thickness of VV tissue in the $C_{2\text{-}3}$ and $C_{4\text{-}5}$ groups was 1.9-fold and 2.1-fold greater, respectively, than that in the CV tissue ($P < .01$; Fig 1). The medial thickness of VV tissue in groups $C_{2\text{-}3}$ and $C_{4\text{-}5}$ was 1.2-fold and 1.3-fold greater, respectively, than that in CV tissue, ($P < .01$; Fig 1). The adventitial thickness of VV tissue in groups $C_{2\text{-}3}$ and $C_{4\text{-}5}$ was 1.8-fold and 2.1-fold greater, respectively, than that of the CV tissue ($P < .05$; Fig 1).

Lipid staining and quantification. In lipid staining with oil red O, the adventitia of the VV tissue showed positive staining, but other regions, such as the intima and media, were not positively stained (Fig 2, *A*). In contrast, no regions of the CV tissue showed positive staining (Fig 2, *A*). These results suggested an unknown mechanism of lipid accumulation in the adventitial tissue of the VV tissue. The PL content in groups $C_{2\text{-}3}$ and $C_{4\text{-}5}$ was higher by 1.8-fold and 1.7-fold, respectively, than in CV tissue ($P < .01$; Fig 2, *B*). In addition, the TG content in groups $C_{2\text{-}3}$ and $C_{4\text{-}5}$ was higher by 2.1-fold and 2.5-fold, respectively, than in the CV tissue ($P < .01$; Fig 2, *B*). The experimental groups did not differ in PL and TG contents (Fig 2, *B*).

Imaging mass spectrometry. We investigated the distribution pattern of lipids in CV and VV tissues using MALDI-IMS (Fig 3, *A*). On gross inspection, there was no notable difference in the patterns between the control and VV groups. Among the spectrum patterns, we paid attention to seven peaks: m/z 496, 782, 798, 804, 820, 879, and 881, which were determined to correspond to LPC (1-acyl 16:0) + H, PC (diacyl 16:0/18:1) + Na, PC (diacyl 16:0/18:1) + K, PC (diacyl 16:0/20:4) + K, TG (52:3) + K and TG (52:2) + K, respectively, based on MS/MS and previous reports using IMS (Table II).

Further analysis using MALDI-IMS revealed that the distribution of LPC (1-acyl 16:0), PC (diacyl 16:0/20:4),

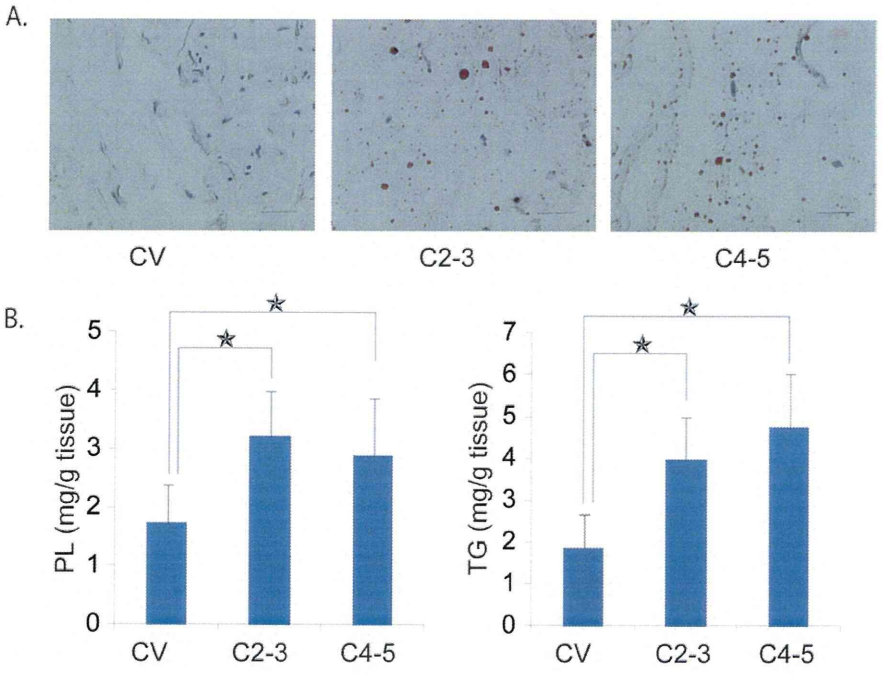

Fig 2. Lipid staining and quantification in vein walls. **A,** Oil red O staining (*bar* = 20 μm). **B,** Lipid content in vein tissue. The phospholipid (*PL*) and triglyceride (*TG*) content of vein walls were compared among the control vein (*CV*) and varicose veins from the CEAP C_{2-3} and C_{4-5} groups. $*P < .05$ indicates a statistically significant difference. The *error bars* show the standard deviation.

TG (52:3), and TG (52:2) in VV tissue differed between each tissue, whereas PC (diacyl 16:0/18:1) was detected ubiquitously in all tissues (Fig 3, *B*). Accumulation of LPC (1-acyl 16:0) and PC (diacyl 16:0/20:4) was found in the VV intima and media. In contrast, accumulation of TG (52:3) and TG (52:2) was found in VV adventitia. However, the distribution patterns of LPC (1-acyl 16:0), PC (diacyl 16:0/20:4), and TG (52:3) and TG (52:2) were similar in the two experimental groups (Fig 3, *B*).

Fig 3, *C* shows quantitative comparisons of LPC (1-acyl 16:0), PC (diacyl 16:0/18:1), PC (diacyl 16:0/20:4), and TG (52:3) and TG (52:2) in the intima, media, and adventitia between CV, C_{2-3} and C_{4-5} tissue as expressed to be a ratio of relative intensity (RRI). RRI was calculated as follows. We designated the intima, media, and adventitia in the region analyzed by IMS as covering the total of ion intensities. The ion intensity obtained from each tissue was not the absolute value. Therefore, each molecule's ion intensity was standardized to that of PC (16:0/18:1) as expressed to be a RRI. PC (16:0/18:1) was widely available for the internal standard molecule at mammalian tissue analysis by IMS.

There were no differences in the RRIs for PC (diacyl 16:0/18:1) among these regions (data not shown). In contrast, the RRIs for LPC (1-acyl 16:0) were significantly higher in the intima, media, and adventitia of VV tissues from the C_{2-3} and C_{4-5} groups compared with controls ($P < .05$; Fig 3, *C*). Similarly, the RRIs for PC (diacyl 16:0/20:4) were significantly higher in the intima, media, and adventitia of C_{2-3} and C_{4-5} VV tissues compared with controls ($P < .05$). The RRIs for TG (52:3) and TG (52:2) in the intima and media of VV tissues were not different from those of CV tissues. However, the RRIs for TG (52:3) and TG (52:2) were significantly higher in the adventitia of VV tissues than in controls ($P < .05$). There were no significant differences in the RRIs for TG (52:3) and TG (52:2) in any tissues between the C_{2-3} and C_{4-5} groups (Fig 3, *C*).

Immunostaining. The vascular endothelial marker von Willebrand factor and a marker specific for lymphatic vessels (D2-40) were applied to the control and VV tissues for visualization of lymphatic vessels. Immunofluorescence staining revealed that lymphatic vessels were present in the adventitia of the GSV in controls and VV tissues (Fig 4, *A*). Significantly fewer lymphatic vessels were seen in complete circumferential sections in the VV groups (C_{2-3} and C_{4-5}) than in controls ($P < .05$; Fig 4, *B*).

DISCUSSION

In this study, the histopathologic changes in structural components of the intima and media (such as collagen, elastin, and smooth muscle) of incompetent GSVs from VV patients are comparable to those previously reported.[14-17] It has been suggested that these changes are due to chronic inflammation in the vein tissue.[14,18-20] Although we showed the increased wall thickness according to the ad-

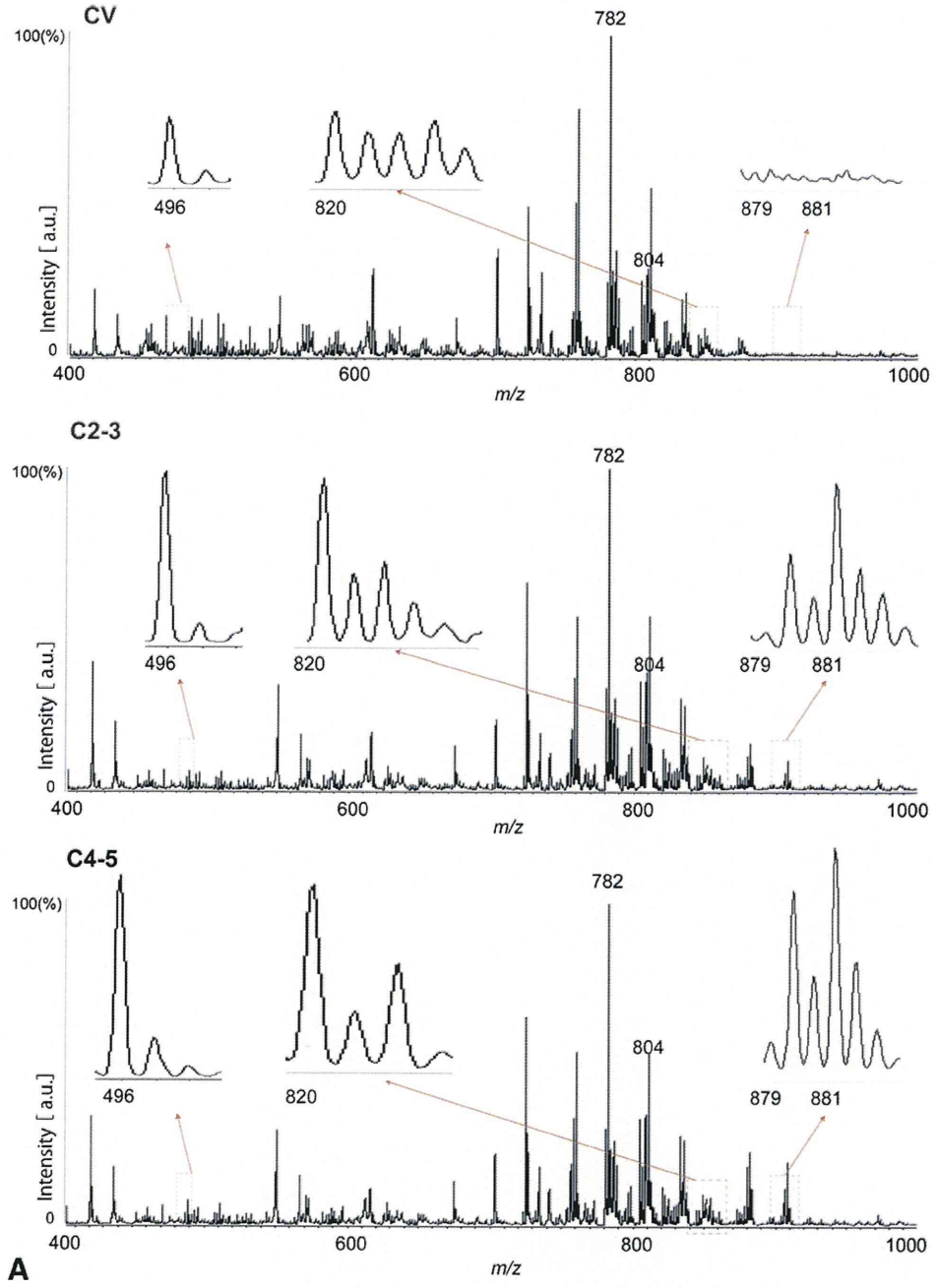

Fig 3. Lipid content analyses by mass spectrometry. **A,** Representative mass spectrum pattern and spectrum of assigned molecule. **B,** Imaging mass spectrometry of vein tissue (*bar* = 200 μm). **C,** The ratio of intensity in vein tissues was compared among control veins (*CV*) and varicose veins from the CEAP $C_{2\text{-}3}$ and $C_{4\text{-}5}$ groups by one-way analysis of variance, followed by the Tukey test. $^{*}P < .05$ indicates a statistically significant difference. $^{\dagger}P < .05$ indicates a statistically significant difference between the $C_{2\text{-}3}$ and $C_{4\text{-}5}$ varicose vein groups. The *error bars* show the standard deviation.

vanced clinical stages, it may be better to use the ratio between the vein wall thickness and the diameter, because wall thickness varies significantly with the size of the vein.

Our previous study was the first to report the abnormal accumulation of lipid molecules in incompetent valve in VVs.[1] In this study, the lipid staining was limited only to the adventitia, and not to the intima and media. We previously reported that lipid staining in the intimal and medial regions was commonly positive in atherosclerotic tissues,[21] which suggested the mechanism of lipid accumulation in

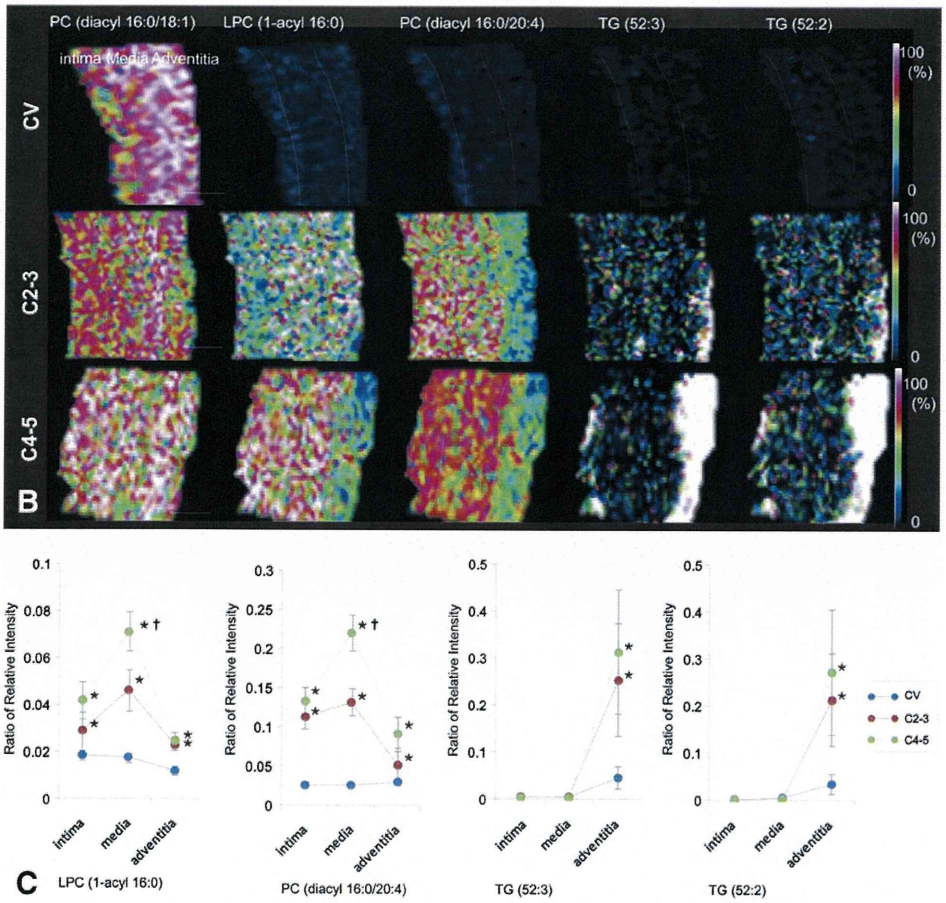

Fig 3. Continued

Table II. Lipid molecule assignments by mass spectrometry

Mass (m)/charge (z)	*Assignment of molecule*
496	LPC (1-acyl 16: 0) + Na
780	PC (diacyl 16:0/18:2) + Na
782	PC (diacyl 16:0/18:1) + Na
796	PC (diacyl 16:0/18:2) + K
798	PC (diacyl 16:0/18:1) + K
804	PC (diacyl 16:0/20:4) + Na
820	PC (diacyl 16:0/20:4) + K
879	Triglyceride (52:3) + K
881	Triglyceride (52:2) + K

LPC, Lysophosphatidylcholine; *PC,* phosphatidylcholine.

the VV tissue seem to be different from that in atherosclerosis. The oil red O staining is a lysochrome diazo dye used for staining of neutral TGs and lipids on frozen sections and some lipoproteins on paraffin sections. To investigate more details of the lipid accumulation and clarify the underlining mechanisms, we applied MALDI-IMS. Unlike conventional biochemical tests that measure lipid content in homogenized tissues or with simple oil red O staining, MALDI-IMS enables the analysis of spatial distributions or specific lipids, along with their fatty acid content, in regions such as the intima, media, and adventitia.

At present, MALDI-IMS is the only method available for the detailed assessment of lipid molecules in tissue. This method distinguishes between different lipid molecular species by simultaneously determining the differences in the mass/charge ratios (*m/z*).

In the present study, PC (diacyl 16:0/20:4) was elevated in all three layers of VV tissues. Although the range of biochemical effects of PC (diacyl 16:0/20:4) is uncertain, elevated levels of the molecule have been reported in mammalian tissues with chronic inflammation.[3,4] We observed that PC (diacyl 16:0/20:4) contains arachidonic acid, which is a precursor to lipid mediators such as proinflammatory prostaglandins and leukotrienes. Taken together, these data indicate that the elevated tissue content of PC (diacyl 16:0/20:4) may be associated with chronic inflammation in the incompetent GSV.

Other studies have reported the occurrence of chronic inflammation in VV tissue.[6,22] LPC (1-acyl 16:0) is known to be a chemotactic factor for macrophages and lymphocytes as well as an inducer of expression of both vascular cell

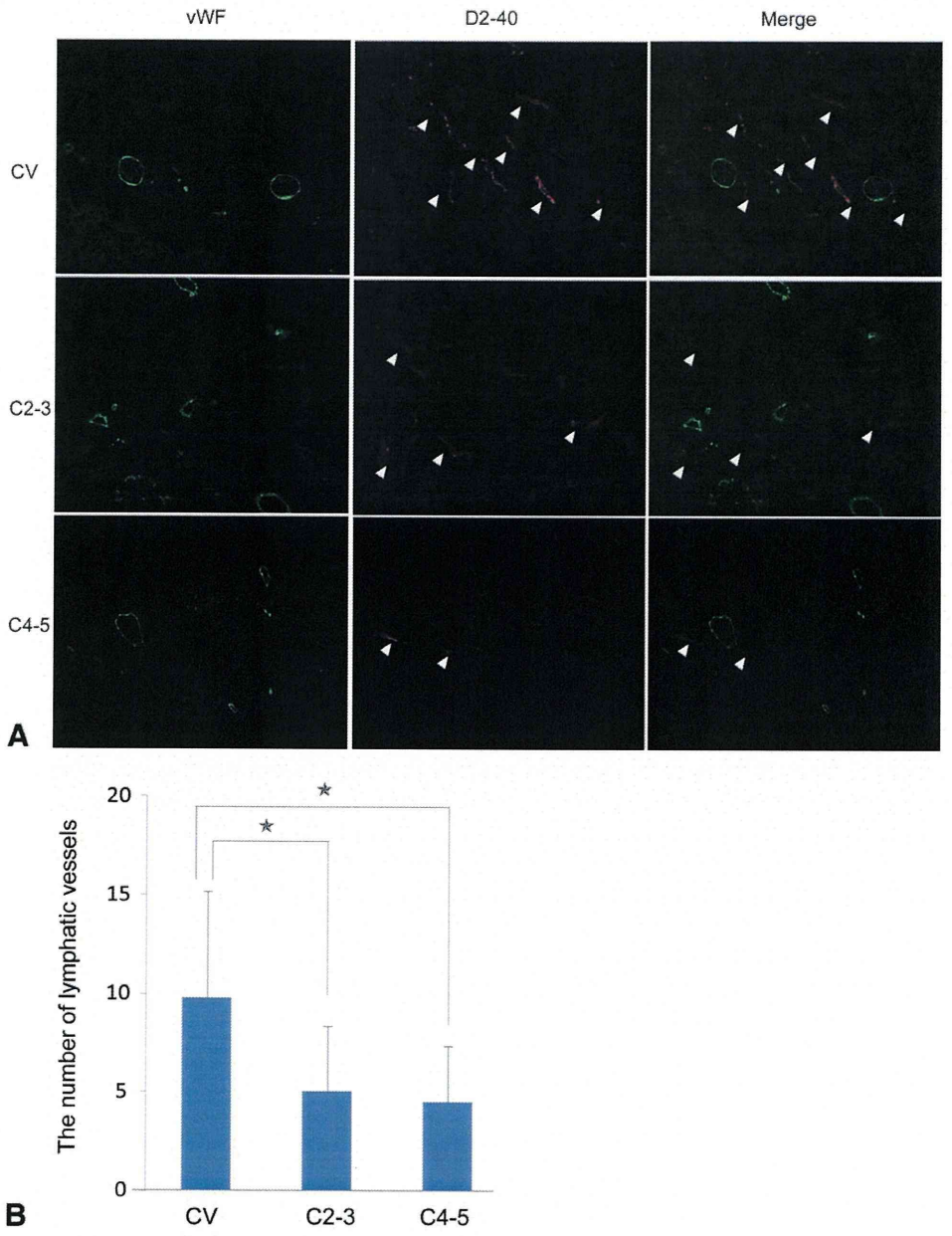

Fig 4. Lymphatic vessel in vein wall. **A,** Immunofluorescent staining for von Willebrand Factor (*green*) and D2-40 (*red; bar* = 20 μm). **B,** Number of lymphatic vessels in complete circumferential sections from each group. **P* < .05 indicates a statistically significant difference. The *error bars* show the standard deviation.

adhesion molecule-1 and intercellular adhesion molecule-1 in endothelial cells.[23] Therefore, LPC (1-acyl 16:0) may also contribute to the chronic inflammation in VV tissue.

Previous studies have highlighted the histologic changes in the intima and media of VV tissues[24,25]; however, adventitial changes have not been reported. The adventitial triglyceride accumulation in VV tissues revealed by MALDI-IMS in this study sheds light on the pathogenesis of the outer surface of the vein wall, which has been previously overlooked. In Fig. 3, *C*, unlike LPC and PC, TG accumulation was limited to the adventitia of the VV tissue. Although LPC, PC, and TG are all lymph ingredients,[26] LPC and PC are also cellular components.[27,28] Therefore, the elevation of LPC and PC in the intima and media might reflect the increase in the number of inflammatory cells in the regions, and lymph stasis (ie, TG accumulation) might be present only in the adventitial regions.

The number of adventitial lymphatic vessels was reduced in the GSV, suggesting that dysfunction of lymph transport and subsequent lymph congestion might occur. Because lymphatic fluid contains high concentrations of lipid molecules, such as PC and TG, lymphatic stasis causes tissue accumulation of lipid molecules.[26,29] Taken together, the abnormal accumulation of various lipid molecules may be associated with disturbances in lymph transport due to the loss of lymph vessels. The association of lymphatic dysfunction with VVs remains to be determined.

Because venodynamics and lymphodynamics interact as an inseparable and mutually dependent dual outflow system in tissue, the system is complex. Homeostasis can only be maintained by a balance between the two systems. The degeneration of VV tissue may be associated with increased permeability, which could cause elevation of tissue pressure and perivascular inflammation. The elevation of tissue pressure induces not only lymphatic vessel dysfunction but also structural damages to the microlymphatic networks.[30]

The resultant lymph stasis is associated with chronic inflammation.[31] Moreover, the inflammation due to cytokines, such as tumor necrosis factor-α, may induce apoptosis of the lymphatic vessel and decrease the number of the vessels.[32] These mixed venous and lymphatic disorders are known as phlebolymphedema.[33,34] In fact, patients with chronic venous insufficiency have microangiopathy of the lymphatic network.[35] We used indocyanine green fluorescence lymphography in a previous study to show that the speed of lymph transportation in the lower leg was reduced in VV patients, suggesting that secondary phlebolymphedema could occur in chronic venous insufficiency.[36] A study that used dynamic lymphoscintigraphy in VV patients reported a similar finding.[37]

The abnormal distribution of lipid molecules in VV tissue observed in both VV groups suggests that VV-associated accumulation of lipid molecules begins in the early clinical stages of the disease and continues through the advanced stages. In particular, the accumulation of LPC (1-acyl 16:0) and PC (diacyl 16:0/20:4) in the media was significantly higher in VV tissue from patients in advanced clinical stages, suggesting an association between lipid accumulation and chronic inflammation of the skin and subcutaneous tissues.

One limitation of this study was that the control veins came from peripheral arterial disease patients, and these veins might have been metabolically affected by the disease. Moreover, GSV from patients with VV might have various histochemical changes, depending on the segments,[38] which would require the harvest of multiple segments of the GSV samples for assessment of the distribution of the lipid molecules.

Further study is needed to clarify the effect of lymph stasis on VVs and chronic inflammation. The mechanism whereby adventitial lymphatic vessels are damaged is also unknown. Consistent venous hypertension and subsequent overload to the lymphatics may account for the lymphatic damage.[30] In addition, accumulation of possible proinflammatory lipid molecules in VV walls may further damage the adventitial lymphatic vessels.

CONCLUSIONS

The accumulation of LPC (1-acyl 16:0) and PC (diacyl 16:0/20:4) in VV tissue may be associated with chronic inflammation, leading to VV tissue degeneration. Moreover, the number of lymphatic vessels in the adventitia of VV tissue is significantly less than that of control tissue. Loss of lymphatic vessels may be associated with the accumulation of lipid molecules and subsequent degeneration of the vein wall in VVs.

We are grateful to Tsuyako Ida, Kinue Hatano, and Yumi Kaneko for their technical assistance.

AUTHOR CONTRIBUTIONS

Conception and design: NU
Analysis and interpretation: HT, NZ, TS, MS
Data collection: HT, NY, NS
Writing the article: HT, NU
Critical revision of the article: HK, MS, NU
Final approval of the article: NU
Statistical analysis: HT
Obtained funding: NU
Overall responsibility: NU

REFERENCES

1. Tanaka H, Zaima N, Yamamoto N, Sagara D, Suzuki M, Nishiyama M, et al. Imaging mass spectrometry reveals unique lipid distribution in primary varicose veins. Eur J Vasc Endovasc Surg 2010;40:657-63.
2. Henriksen JR, Andresen TL, Feldborg LN, Duelund L, Ipsen JH. Understanding detergent effects on lipid membranes: a model study of lysolipids. Biophys J 2010;98:2199-205.
3. Koizumi S, Yamamoto S, Hayasaka T, Konishi Y, Yamaguchi-Okada M, Goto-Inoue N, et al. Imaging mass spectrometry revealed the production of lyso-phosphatidylcholine in the injured ischemic rat brain. Neuroscience 2010;168:219-25.
4. Yang HJ, Ishizaki I, Sanada N, Zaima N, Sugiura Y, Yao I, et al. Detection of characteristic distributions of phospholipid head groups and fatty acids on neurite surface by time-of-flight secondary ion mass spectrometry. Med Mol Morphol 2010;43:158-64.
5. Lim CS, Davies AH. Pathogenesis of primary varicose veins. Br J Surg 2009;96:1231-42.
6. Bergan JJ, Pascarella L, Schmid-Schönbein GW. Pathogenesis of primary chronic venous disease: insights from animal models of venous hypertension. J Vasc Surg 2008;47:183-92.
7. Eklöf B, Rutherford RB, Bergan JJ, Carpentier PH, Gloviczki P, Kistner RL, et al. Revision of the CEAP classification for chronic venous disorders: consensus statement. J Vasc Surg 2004;40:1248-52.
8. Yamamoto N, Unno N, Mitsuoka H, Saito T, Miki K, Ishimaru K, et al. Preoperative and intraoperative evaluation of diameter-reflux relationship of calf perforating veins in patients with primary varicose vein. J Vasc Surg 2002;36:1225-30.
9. Shrivas K, Hayasaka T, Goto-Inoue N, Sugiura Y, Zaima N, Setou M. Ionic matrix for enhanced MALDI imaging mass spectrometry for identification of phospholipids in mouse liver and cerebellum tissue sections. Anal Chem 2010;82:8800-6.
10. Morita Y, Ikegami K, Goto-Inoue N, Hayasaka T, Zaima N, Tanaka H, et al. Imaging mass spectrometry of gastric carcinoma in formalin-fixed paraffin-embedded tissue microarray. Cancer Sci 2010;101:267-73.
11. Hayasaka T, Goto-Inoue N, Zaima N, Kimura Y, Setou M. Organ-specific distributions of lysophosphatidylcholine and triacylglycerol in mouse embryo. Lipids 2009;44:837-48.

12. Sugiura Y, Konishi Y, Zaima N, Kajihara S, Nakanishi H, Taguchi R, et al. Visualization of the cell-selective distribution of PUFA-containing phosphatidylcholines in mouse brain by imaging mass spectrometry. J Lipid Res 2009;50:1776-88.
13. Zaima N, Sugawara T, Goto D, Hirata T. Trans geometric isomers of EPA decrease LXRalpha-induced cellular triacylglycerol via suppression of SREBP-1c and PGC-1beta. J Lipid Res 2006;47:2712-7.
14. Elsharawy MA, Naim MM, Abdelmaguid EM, Al-Mulhim AA. Role of saphenous vein wall in the pathogenesis of primary varicose veins. Interact Cardiovasc Thorac Surg 2007;6:219-24.
15. Wali MA, Eid RA. Smooth muscle changes in varicose veins: an ultrastructural study. J Smooth Muscle Res 2001;37:123-35.
16. Xiao Y, Huang Z, Yin H, Lin Y, Wang S. In vitro differences between smooth muscle cells derived from varicose veins and normal veins. J Vasc Surg 2009;50:1149-54.
17. Travers JP, Brookes CE, Evans J, Baker DM, Kent C, Makin GS, et al. Assessment of wall structure and composition of varicose veins with reference to collagen, elastin and smooth muscle content. Eur J Vasc Endovasc Surg 1996;11:230-7.
18. Meissner MH, Gloviczki P, Bergan J, Kistner RL, Morrison N, Pannier F, et al. Primary chronic venous disorders. J Vasc Surg 2007;46(Suppl S):54-67S.
19. Rizzi A, Quaglio D, Vasquez G, Mascoli F, Amadesi S, Calò G, et al. Effects of vasoactive agents in healthy and diseased human saphenous veins. J Vasc Surg 1998;28:855-61.
20. Wali MA, Eid RA. Changes of elastic and collagen fibers in varicose veins. Int Angiol 2002;21:337-43.
21. Zaima N, Sasaki T, Tanaka H, Cheng XW, Onoue K, Hayasaka T, et al. Imaging mass spectrometry-based histopathologic examination of atherosclerotic lesions. Atherosclerosis 2011;217:427-32.
22. Pascarella L, Schmid-Schönbein GW, Bergan J. An animal model of venous hypertension: the role of inflammation in venous valve failure. J Vasc Surg 2005;41:303-11.
23. Kume N, Gimbrone MA, Jr. Lysophosphatidylcholine transcriptionally induces growth factor gene expression in cultured human endothelial cells. J Clin Invest 1994;93:907-11.
24. Lim CS, Gohel MS, Shepherd AC, Paleolog E, Davies AH. Venous hypoxia: a poorly studied etiological factor of varicose veins. J Vasc Res 2011;48:185-94.
25. Takase S, Pascarella L, Bergan JJ, Schmid-Schönbein GW. Hypertension-induced venous valve remodeling. J Vasc Surg 2004;39:1329-34.
26. Nanjee MN, Cooke CJ, Olszewski WL, Miller NE. Lipid and apolipoprotein concentrations in prenodal leg lymph of fasted humans. Associations with plasma concentrations in normal subjects, lipoprotein lipase deficiency, and LCAT deficiency. J Lipid Res 2000;41:1317-27.
27. Liu E, Goldhaber JI, Weiss JN. Effects of lysophosphatidylcholine on electrophysiological properties and excitation-contraction coupling in isolated guinea pig ventricular myocytes. J Clin Invest 1991;88:1819-32.
28. Balsinde J, Dennis EA. Function and inhibition of intracellular calcium-independent phospholipase a2. J Biol Chem 1997;272:16069-72.
29. Bennuru S, Maldarelli G, Kumaraswami V, Klion AD, Nutman TB. Elevated levels of plasma angiogenic factors are associated with human lymphatic filarial infections. Am J Trop Med Hyg 2010;83:884-90.
30. Zawieja DC. Contractile physiology of lymphatics. Lymph Res Biol 2009;7:87-96.
31. Tabibiazar R, Cheung L, Han J, Swanson J, Beilhack A, An A, et al. Inflammatory manifestations of experimental lymphatic insufficiency. PLoS Med 2006;3:e254.
32. Niemann-Jönsson A, Ares MP, Yan ZQ, Bu DX, Fredrikson GN, Brånén L, et al. Increased rate of apoptosis in intimal arterial smooth muscle cells through endogenous activation of TNF receptors. Arterioscler Thromb Vasc Biol 2001;21:1909-14.
33. Bunke N, Brown K, Bergan BJ. Phlebolymphemeda: usually unrecognized, often poorly treated. Perspect Vasc Surg Endovasc Ther 2009;21:65-8.
34. Piller N. Phlebolymphoedema/chronic lymphatic insufficiency: an introduction to strategies for detection, differentiation and treatment. Phlebology 2009;24:51-5.
35. Franzeck UK, Haselbach P, Speiser D, Bollinger A. Microangiopathy of cutaneous blood and lymphatic capillaries in chronic venous insufficiency (CVI) Yale. J Biol Med 1993;66:37-46.
36. Suzuki M, Unno N, Yamamoto N, Nishiyama M, Sagara D, Tanaka H, et al. Impaired lymphatic function recovered after great saphenous vein stripping in patients with varicose vein: venodynamic and lymphodynamic results. J Vasc Surg 2009;50:1085-91.
37. Mortimer PS. Evaluation of lymphatic function: Abnormal lymph drainage in venous disease. Int Angiol 1995;14:32-5.
38. Badier-Commander C, Couvelard A, Henin D, Verbeuren T, Michel JB, Jacob MP. Smooth muscle cell modulation and cytokine overproduction in varicose veins. An in situ study J Pathol 2001;193:398-407.

Submitted Aug 7, 2011; accepted Sep 17, 2011.

analytical chemistry

ARTICLE

pubs.acs.org/ac

Method for Simultaneous Imaging of Endogenous Low Molecular Weight Metabolites in Mouse Brain Using TiO_2 Nanoparticles in Nanoparticle-Assisted Laser Desorption/Ionization-Imaging Mass Spectrometry

Kamlesh Shrivas, Takahiro Hayasaka, Yuki Sugiura, and Mitsutoshi Setou*

Department of Cell Biology and Anatomy, Hamamatsu University School of Medicine, 1-20-1 Handayama, Higashi-ku, Hamamatsu, Shizuoka 431-3192, Japan

Supporting Information

ABSTRACT: We report the detection of a group of endogenous low molecular weight metabolites (LMWM) in mouse brain (80−500 Da) using TiO_2 nanoparticles (NPs) in nanoparticle-assisted laser desorption/ionization-imaging mass spectrometry (Nano-PALDI-IMS) without any washing and separation step prior to MS analysis. The identification of metabolites using TiO_2 NPs was compared with a conventional organic matrix 2,5-dihydroxybenzoic acid (DHB) where signals of 179 molecules were specific to TiO_2 NPs, 4 were specific to DHB, and 21 were common to both TiO_2 NPs and DHB. The use of TiO_2 NPs enabled the detection of a higher number of LMWM as compared to DHB and gold NPs as a matrix. This approach is a simple, inexpensive, washing, and separation free for imaging and identification of LMWM in mouse brain. We believe that the biochemical information from distinct regions of the brain using a Nano-PALDI-IMS will be helpful in elucidating the imbalances linked with diseases in biomedical samples.

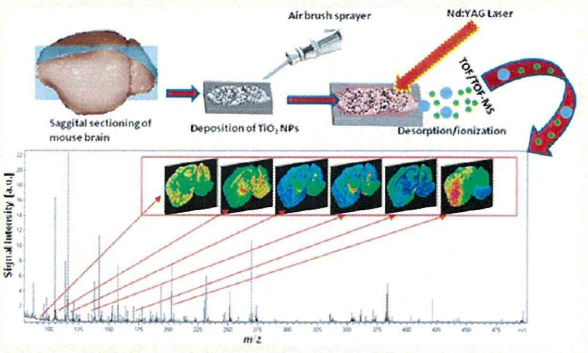

The brain is the central part of the nervous system, and it monitors and regulates the body's actions and reactions. The presence of endogenous low molecular weight metabolites (LMWM) in brain has important role in biosynthesis, product degradation, energy production, signaling, and defense.[1] Recent advances in molecular imaging modalities have opened opportunities for molecular diagnostic and therapeutic procedures. Magnetic resonance imaging (MRI) and positron emission tomography (PET) are known noninvasive techniques in imaging for medical diagnosis and also used for obtaining biochemical information from living tissue in order to establish the presence of any disorder.[2,3] Nuclear magnetic resonance spectroscopy (NMRS) imaging is also helpful for the identification of LMWM in brain. So far, with NMRS imaging, only a few molecules are reported which are highly abundant in the brain.[4] The limitations of these techniques are relatively poor resolution, sensitivity, and requirement of labeling of molecules for the detection (in the case of PET method). Liquid chromatography−mass spectrometry (LC-MS) is normally used for the analysis of LMWM in tissue samples.[5] Petyuk et al. demonstrated the mapping of abundance protein in brain using voxelation in combination with LC-MS. This approach provided a procedure to image the brain proteome in the adult and also to understand the etiology of neurodegenerative and other brain disorders.[6] However, this technique requires tedious sample preparation and longer analysis time.

Nowadays, matrix-assisted laser desorption/ionization mass spectrometry (MALDI-MS) is proven to be a simple and rapid tool available to researchers in biochemistry and molecular biology for the identification of biomolecules.[7] However, the analysis of LMWM (<500 Da) is limited in MALDI-MS applications because of the organic matrix-oriented low mass interferences. Therefore, inorganic and nanomaterials are introduced as the matrix in order to reduce the drawbacks of organic matrixes in the MALDI-MS analysis. Tanaka et al. first reported the application of a 30 nm diameter cobalt powder suspended in glycerol in MALDI-MS for the analysis of protein molecules where the nanoparticles (NPs) are used for desorption and ionization of analytes.[8] Sunner et al. demonstrated the use of graphite microparticles of size 2−200 μm mixed with glycerol as the matrix for the analysis of proteins and peptides, and the procedure is known as a surface-assisted laser desorption/ionization mass spectrometry (SALDI-MS).[9] Later, Wei et al. introduced a matrix free method known as a desorption/ionization on silicon (DIOS) produced by electrochemical etching of silicon surface to ionize the small molecules with no or little chemical background mass signal in the mass spectra.[10] The use of TiO_2 NPs in MALDI-MS

Received: March 10, 2011
Accepted: August 19, 2011
Published: September 06, 2011

has also been reported for desorption and ionization of biomolecules. Lee et al. applied TiO_2 NPs as a matrix for the determination of enediol compounds in tea.[11] Watanabe et al. investigated the photocatalytic cleaning on SALDI-MS with amorphous TiO_2 NPs for the reduction of the background noise and the improvement of the sensitivity of peptides.[12] In addition, gold (Au) NPs are reported for the analysis of a low molecular weight molecule (i.e., glutathione) in SALDI-MS.[13] However, the use of AuNPs as a matrix in SALDI-MS for analysis of small molecules (in the range of 80−500 Da.) showed NP-oriented peaks in the mass spectrum which might affect the sensitivity for the detection of molecules in MS.[14]

As a result of recent advances in nanomaterial preparation, nanomaterial surfaces are used in MALDI imaging mass spectrometry (IMS) for identification and localization of biomolecules in different types of tissue sections. Siuzdak's group has introduced a matrix-free desorption/ionization platform for imaging of biomolecules in tissue samples and named "nanostructure-initiator mass spectrometry (NIMS)".[15] There are other approaches, such as graphite-assisted laser desorption/ionization (GALDI)[16] and DIOS reported for the identification of organic compounds from the tissue surface. Recently, Nanoassisted laser desorption/ionization (NALDI) target plate was introduced for imaging and identification of lipids in mouse brain with very low chemical background.[17] In this scenario, our group has developed a method called nanoparticle-assisted laser desorption/ionization imaging mass spectrometry (Nano-PALDI-IMS) for cellular resolution of cerebellum tissue section to visualize peptides, phospholipids, and metabolites.[18] More recently, silver[19] and gold[20] NPs are used in Nano-PALDI-IMS to identify different types of fatty acids and glycosphingolipids, respectively, in mouse tissue samples which are hardly identified using 2,5-dihydroxybenzoic acid (DHB) as a matrix. However, the simultaneous imaging and detection of LMWM (<500 Da) other than lipid and peptide molecules in biomaterial is still a great challenge at this cutting edge of chemistry and biology.

In the present work, TiO_2 NPs are used as a nanomaterial surface to absorb laser light for effective desorption and ionization of biomolecules in mouse brain using Nano-PALDI-IMS without observing any NP related peaks. TiO_2 NPs are active photocatalytic NPs and have been widely applied in analytical, biochemical, and nanoscience fields.[21] TiO_2 NPs exhibit strong absorption characteristics in the UV region which can be used as a matrix for desorption and ionization of biomolecules.[21,22] The identification of LMWM in tissue sample using TiO_2 NPs is compared with use of DHB and gold NPs as matrixes. MS/MS and capillary electrophoresis mass spectrometry (CE-MS) measurements[23] were also performed on the tissue samples to confirm some of the metabolites found in the brain. The localization patterns of 24 LMWM in mouse brain were demonstrated. The usefulness of the method was also implemented to show the calibration curve for model compound, histidine on the surface of tissue section.

EXPERIMENTAL SECTION

Chemicals. Trifluoroacetic acid (TFA) and titanium(IV) *n*-butoxide were obtained from Sigma (St. Louis, MO). DHB was purchased from Bruker Daltonics (Bremen, Germany). Diammonium hydrogen citrate was obtained from Nacalai Tesque Inc. (Kyoto, Japan). Citric acid and methanol were obtained from Wako Pure Chemicals (Osaka, Japan).

Synthesis of TiO_2 and AuNPs NPs. TiO_2 NPs were prepared as the previously described hydrolysis of titanium(IV) *n*-butoxide in water and ethanol in acidic condition.[21] Briefly, 17 mL of titanium(IV) *n*-butoxide and 8 mL of ethanol were mixed by stirring for 10 min at room temperature. Then, a solution containing 8 mL of ethanol and 375 μL of nitric acid was added dropwise to stirred titanium(IV) *n*-butoxide and solution which was cooled in an ice/water bath under stirring. The concentration of obtained solution of TiO_2 NPs was found to be 1.48 M (Supporting Information). The lower concentrations of NPs (2.42−12.13 mM) were prepared for analysis of mouse brain tissue sections for Nano-PALDI-IMS experiments. The size of the TiO_2 NPs was confirmed using a transmission electron microscope, TEM (JEM 1010), at an accelerating voltage of 80 kV. The TEM image TiO_2 NPs are shown in Supporting Information, Figure S1. AuNPs were synthesized according to ref 14 (Supporting Information).

Solution Preparations. A 97−485 mM DHB solution was prepared by dissolving an appropriate amount of DHB in 1 mL of 75% methanol (containing 0.1% TFA) for MALDI-IMS analysis. Different concentrations of TiO_2 NPs in the range of 2.42−12.13 mM were prepared in 1 mL of methanol from 1.48 M TiO_2 NPs with addition of citrate buffer, 60 μL of diammonium hydrogen citrate (50 mM), and 20 μL of citric acid (100 mM) for Nano-PALDI-IMS analysis. The citrate buffer was added into the TiO_2 NPs to assist the protonation of molecules in MS. Safety steps were maintained during the handling of organic solvents and chemicals used in the experiments.

Preparation of Mouse Brain Tissue Sections. Experimental procedures for mouse samples were performed in accordance with the Animal Experiment Regulations of Hamamatsu University School of Medicine approved by the Science Council of Japan. A male mouse was obtained from Japan SLC (Shizuoka, Japan) and was anesthetized prior to being decapitated. Brain was dissected and frozen in liquid nitrogen and then stored at −80 °C until sectioning of sample. The 15 μm-thick mouse brain tissues were sliced using a cryostat (CM 1950; Leica Microsystems, Wetzler, Germany) at −20 °C, and sections were thaw mounted on indium-tin-oxide (ITO)-coated glass slides. One milliliter of prepared solution of TiO_2 NPs and DHB matrix solution was sprayed on the surface of brain tissue sections using a 0.2 mm nozzle caliber airbrush (Procon Boy FWA Platinum, Tokyo) for MALDI imaging of metabolites.

IMS, MS/MS, and CE-MS Analyses. Imaging of LMWM in mouse brain was performed by an ultraflex II TOF/TOF (Bruker Daltonics) equipped with a 355 nm Nd:YAG laser with a 200 Hz repetition rate. The laser energy used in Nano-PALDI- and MALDI-IMS analyses was 100 μJ. The parameters, such as laser energy, detector gain, and random walk function were first optimized to obtain good sensitivity of the target molecules from the samples. flexImaging software (Version 3.0 obtained from Bruker Daltonics) was used to reconstruct ion images of metabolites at m/z from a whole tissue average spectrum. The mass peaks (at m/z) obtained were normalized to total ion current, and then, peak intensity was taken in account to study the distribution of molecules in tissue section. Before performing the MALDI imaging experiment in TOF/TOF-MS, the instrument was calibrated with DHB, bradykinin, and angiotensin II at m/z 155.03 $[M+H]^+$, 757.39 $[M+H]^+$, and 1046.54 $[M+H]^+$ in the positive ion mode. The mixture of DHB, bradykinin, and angiotensin II was deposited near to the brain tissue section for calibration of the instrument in order to avoid the mass error

dx.doi.org/10.1021/ac201602s |Anal. Chem. 2011, 83, 7283–7289

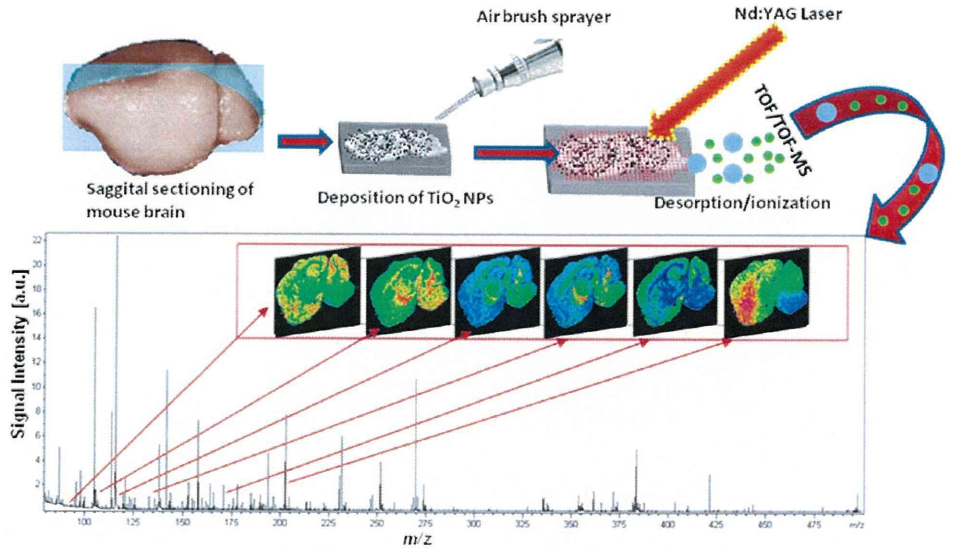

Figure 1. Work flow of Nano-PALDI-IMS experiment. The 15 μm-thick mouse brain tissues were sliced using a cryostat and thaw mounted on ITO coated glass slides, and the TiO_2 NPs were applied on the surface of tissue section and followed by Nano-PALDI-IMS analyses.

for extended and uneven tissue section prior to imaging. We also confirmed the MS/MS analyses of LMWM in mouse brain tissue section using Q-TOF-MS. Capillary electrophoresis (CE)-MS based analyses were performed for confirmation of LMWM using Agilent CE systems equipped with a time-of-flight mass spectrometer (TOF-MS) and a built-in diode-array detector (Agilent Technologies). The details of sample preparation, capillary type, and instrumental conditions can be found in the Supporting Information.[23]

Sample-to-Sample Reproducibility in Mouse Tissue. Sample-to-sample reproducibility for Nano-PALDI-IMS and MALDI-IMS analyses of LMWM were calculated in terms of relative standard deviation percentage (±RSD,%) which presented the precision of the proposed method. For this, 0.2 μg/mm^3 of histidine was deposited on the three serial section of brain tissue (n = 3), and imaging experiments were performed using TiO_2 NPs and DHB as a matrix. The region of interest (ROI) was selected from triplicate analyses, and mean intensity was used to calculate the RSD, %. The calculation for RSD % of TiO_2 NPs and DHB is given in the Supporting Information.

Quantitative Analysis of Histidine in Mouse Tissue. To establish a calibration curve, different concentrations of histidine (0.1, 0.2, 0.4, 0.8, and 1.6 μg/mm^3) were spotted on the surface of brain tissue section and TiO_2 NPs were deposited using an airbrush followed by Nano-PALDI-IMS. The number of analyses of tissue sections was performed three times (n = 3) at each concentration. The region of interest (ROI) selected and average intensity from each concentration of histidine (at m/z 156.08) was exported using a script program (included in the flexAnalysis, Bruker Daltonics). The average intensity (n = 3) of each concentration was used to construct the calibration curve for histidine in tissue section.

RESULTS AND DISCUSSION

In the present work, Nano-PALDI-IMS was applied for simultaneous imaging of LMWM (<500 Da) in brain tissue after applying TiO_2 NPs on the surface of tissue section for effective desorption and ionization of molecules. TiO_2 NPs has been widely used as a transition-metal oxide, which is characterized by a filled valence band and an empty conduction band. Thus, the laser energy absorbed by TiO_2 NPs is most likely converted to thermal energy through the formation of charge carrier and then transferred to the top layer of the tissue surface for the desorption/ionization process.[22,24] Molecules present on the discrete spots or the pixel are ionized using laser energy in the raster fashion. Figure 1 shows the work flow of the Nano-PALDI-IMS imaging experiment.

Analysis of Mouse Brain. Mouse brain was selected for imaging of LMWM in tissue section using TiO_2 NPs as a matrix for desorption/ionization of molecules. Figure 2a represents the sagittal section of HE-stained mouse brain showing cerebellar cortex (CBX), corpus striatum (CP), cerebral cortex (CTX), hippocampus formation (HPF), and thalamus (TH). TiO_2 NPs (Figure 2b) and DHB (Figure 2c) were deposited on the surface of brain tissue sections and analyzed at a scan pitch of 70 μm in the positive ion mode followed by the reconstruction of ion images. The regions of mouse brain could be differentiated after the deposition of TiO_2 NPs due to the formation of a very thin layer of coating of NPs on the surface of a tissue section as the size of NPs was <10 nm. Conversely, the structure of mouse brain can be hardly examined after the deposition of DHB matrix due to the thick layer deposition of matrix on the surface of the tissue section (crystal size of the matrix is found to be 50 μm).[25]

The ionization efficiency of analyte molecules greatly depends on the concentration of NPs and DHB matrixes used in SALDI-MS[14] and MALDI-MS, respectively. Thus, the concentrations of TiO_2 NPs and DHB matrix were optimized for efficient desorption/ionization of molecules from the surface of brain tissue (Supporting Information, Figures S2 and S3). The mass spectra of LMWM obtained using TiO_2 NPs and DHB as a matrix are shown in Figure 3a,b, respectively. In Figure 3a, the ion signals were generated at m/z 137.01, 155.03, 177.04, 230.05, 273.02, 352.78, and 382.76 which are corresponding to $[DHB - H_2O + H]^+$, $[DHB + H]^+$, $[DHB + Na]^+$, $[DHB + 2K - H]^+$, $[2DHB - 2H_2O + H]^+$, $[2DHB + 2Na - H]^+$, and $[2DHB + 2K - H]^+$,

dx.doi.org/10.1021/ac201602s |Anal. Chem. 2011, 83, 7283–7289

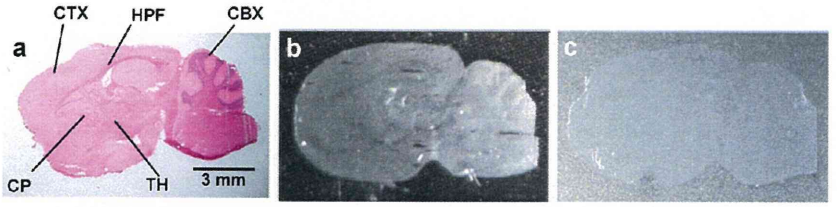

Figure 2. Sagittal section of mouse brain (a): HE-stained mouse brain showing cerebellar cortex (CBX), corpus striatum (CP), cerebral cortex (CTX), hippocampus formation (HPF), and thalamus (TH). (b) Deposited with TiO_2 NPs. (c) Deposited with DHB matrix, with 3 mm scale bar (black color line).

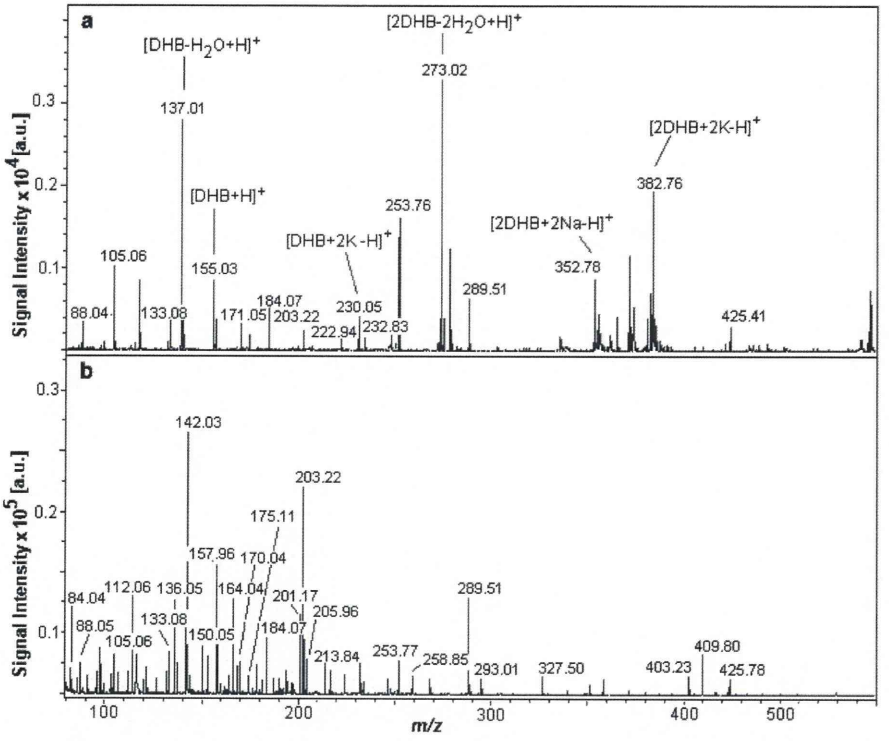

Figure 3. Mass spectra of LMWM in detected in mouse brain tissue section obtained with (a) DHB in MALDI-IMS and (b) TiO_2 NPs in Nano-PALDI-IMS.

respectively. The signals produced from DHB in MALDI-MS might influence both the interpretation of metabolites in mass spectra and the sensitivity for the detection. Less than 25 biomolecule signals were obtained using DHB as a matrix. However, 200 biomolecule signals with higher signal intensity were observed using TiO_2 NPs without any NP related peaks, shown in Figure 3b. The control experiment was also performed by depositing TiO_2 NPs on the ITO glass slide and no any NP-oriented peaks were observed in the mass spectrum (Supporting Information, Figure S4). The mass peaks (m/z) obtained in the mass spectrum were reconstructed to form ion images using flexImaging software. We were able to reconstruct the distribution of metabolites in mouse brain where 179 molecule signals were specific to TiO_2 NPs (Figure 4a and Supporting Information, Figure S5a–c); 4 were specific to DHB (Supporting Information, Figure S6); and 21 were common to both TiO_2 NPs and DHB matrix (Figure 4b and Supporting Information, Figure S7). We also analyzed a standard compound such as serine, cysteine, and tyrosine to check the fragmentation of any detected molecules in brain tissue section using TiO_2 NPs at the same laser energy (100 μJ) used for the IMS experiments. For this, 1 μL of serine, cysteine, and tyrosine (50 ng/μL) with the same amount of NPs were deposited on the target plate followed by the MS analysis. The results showed no fragmentation of molecules in the mass spectrum when TiO_2 NPs was used as a matrix (Supporting Information, Figure S8a–c). This enabled us to conclude that the use of TiO_2 NPs is effective for ionization of biomolecules from the surface of brain tissue.

Localization of LMWM in Mouse Brain. The selected ion images of metabolites in Figure 4 showed the structure of mouse brain with distinguishable localization of ion distribution in different compartments of the brain section. The ion images found for putrescine at m/z 89.10 $[M + H]^+$, γ-aminobutyric acid at m/z 104.06 $[M + H]^+$, uracil at m/z 113.03 $[M + H]^+$, ornithine at m/z 133.08 $[M + H]^+$, and hypoxanthine at m/z 137.05 $[M + H]^+$ were specific to gray matter region of the mouse brain which

dx.doi.org/10.1021/ac201602s |Anal. Chem. 2011, 83, 7283–7289

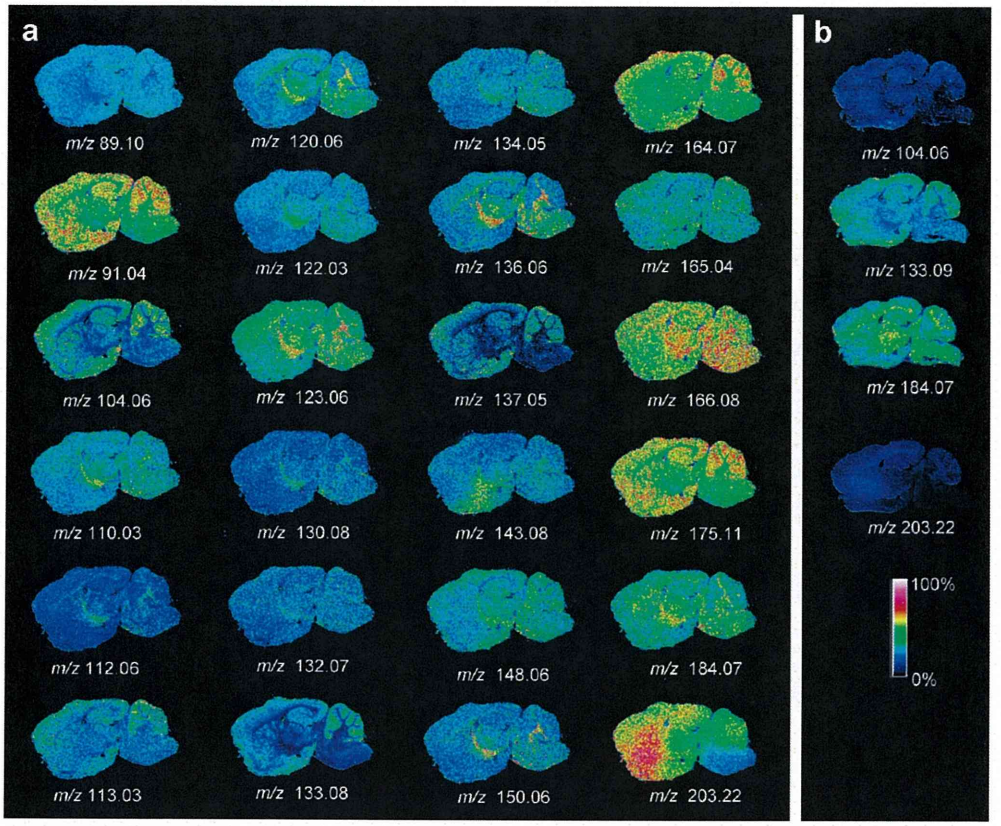

Figure 4. Ion images of LMWM in mouse brain obtained with (a) TiO_2 NPs in Nano-PALDI-MS and (b) DHB matrix in MALDI-MS.

exhibited almost the same type of ion distribution. The white matter of the mouse brain can be differentiated by ion images of cytosine at m/z 112.06 $[M + H]^+$, threonine at m/z 120.06 $[M + H]^+$, pipecolic acid at m/z 130.08 $[M + H]^+$, adenine at m/z 136.06 $[M + H]^+$, and phenylalanine at m/z 166.08. The lobular structure of the cerebellum can be distinguished by ion images of γ-aminobutyric acid at m/z 104.06 $[M + H]^+$, ornithine at m/z 133.08 $[M + H]^+$, hypoxanthine at m/z 137.05 $[M + H]^+$, and *S*-methylmethionine at m/z 164.07. The most intense ion was observed at the striatum region of the mouse brain for spermine at m/z 203.22 $[M + H]^+$, and some white matter specific region was examined for phosphorylcholine at m/z 184.07 $[M]^+$ in thalamus and cerebellum, whereas the creatine acid at m/z 132.07 $[M + H]^+$ showed almost an uniform distribution of ions across the tissue section. This data set indicates the region-specific studies of LMWM and provides important information for performing such analyses in mouse brain.

MS/MS and CE-MS Analysis of LMWM in Mouse Brain. MS/MS analyses of five molecules, such as, γ-aminobutyric acid, phosphorylcholine, cytosine, threonine, and creatine, in positive ion mode are illustrated in the Supporting Information, Figures S9–S13. Other assigned molecules were validated using CE-MS compared with respective standard compounds (Supporting Information, Table S1). The detected molecules in brain tissue sample were matched against known Human Metabolome Database Search maintained Genome Alberta and Genome Canada (http://www.hmdb.ca) and KEGG GenomeNet Database Resources (http://www.genome.jp).

Reproducibility and Quantitative Analysis. Sample-to-sample reproducibility (RSD) obtained for analysis of histidine in tissue section was ±12.1 and ±26.7% using TiO_2 NPs and DHB matrix, respectively. A higher percentage of RSD (±26.7%) showed a large variation of signal height when DHB matrix was used as a matrix probably due to the heterogeneous crystal formation of matrix with sample. However, a lower value of RSD (±12.1%) represented a small variation in signal intensity during the imaging of LMWM using NPs, possibly due to the homogeneous thin crystal formation of NPs on the surface of tissue. This heterogeneous distribution of DHB crystals and uniform distribution of NPs was also reported by Taira et al., in Nano-PALDI-IMS analysis of biomolecules.[18] From these results, we can conclude that a good value of sample reproducibility was obtained when TiO_2 NPs as a matrix was compared to DHB in IMS analyses. Thus, the TiO_2 NPs were demonstrated for quantitative analysis of histidine from the surface of tissue section. The ion images for different concentrations of histidine obtained from the brain tissue section are shown in Figure 5a. The linear range for histidine was found between 0.1 and 1.6 $\mu g/mm^3$ with the correlation of estimation <0.998, shown in Figure 5b. This suggests that the quantitative analysis can be performed using a Nano-PALDI-IMS for the determination of LMWM in brain tissue sample.

Comparison for Imaging of LMWM in Mouse Brain Using TiO_2 NPs, DHB, and AuNPs as a Matrix. We compared the identification of LMWM using TiO_2 NPs in Nano-PALDI-IMS with MALDI-IMS using DHB matrix. Figure 4a,b and Figure S7 (Supporting Information) show the ion images of LMWM in the mouse brain tissue section using TiO_2 NPs and DHB as a matrix. A number of LMWM with good signal intensity were obtained

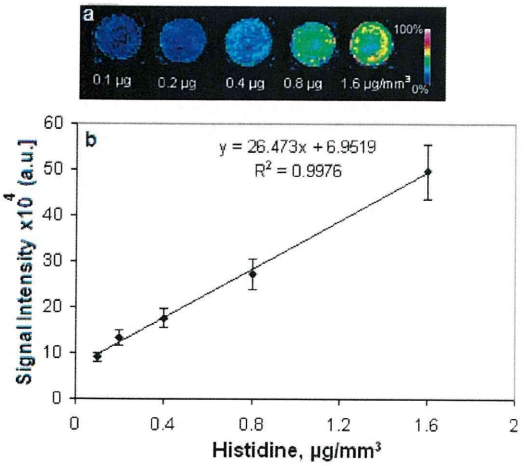

Figure 5. Ion images of histidine (at 0.1, 0.2, 0.4, 0.8, and 1.6 $\mu g/mm^3$) obtained from the brain tissue section using Nano-PALDI-IMS (a). The linear range for histidine was found between 0.1 and 1.6 $\mu g/\mu m^3$ with the correlation of estimation <0.9977 (b). The error bar represented as the mean ± standard deviation (n = 3).

when TiO_2 NPs was used as a matrix in Nano-PALDI-IMS as compared to the use of DHB in MALDI-IMS analysis. The reason for obtaining a higher signal intensity and number of metabolites using TiO_2 NPs is due to the thin coating of NPs on the surface of the brain tissue section that may have caused an efficient absorption and transfer of the light energy for desorption and ionization of molecules from the surface of tissue section. Taira et al. also reported the detection of a higher number of biomolecules from the surface of tissue sample when a small size of NPs was used as a matrix in Nano-PALDI-IMS.[18] The biomolecules at m/z 104.06, 133.08, 184.07, and 203.22 (shown in Figure 4) were detected by both approaches where the distribution of ion pattern were found to be same, though the signal intensity of ion images formed using DHB was less intense than that using the TiO_2 NPs. These results confirmed the ability of TiO_2 NPs in detecting a number of molecule signals in brain tissue when used in Nano-PALDI-IMS.

In addition, we also performed an imaging of mouse brain without use of TiO_2 NPs in laser desorption ionization (LDI-MS) and AuNPs in SALDI-MS to detect a LMWM from the tissue section at the same laser energy used in the Nano-PALDI-IMS experiments. LDI-MS is reported to be a matrix free technique for analysis of low molecular biomolecules from tissue surface. However, when LDI-IMS (without use of TiO_2 NPs as a matrix) was applied for analysis of biomolecules, no signal was detected from the surface of mouse brain tissue. Next, we applied AuNPs on the surface of brain tissue section and IMS analysis was performed at the optimal conditions. Figure S14 (Supporting Information) shows the mass spectrum of LMWM in tissue section using AuNPs for desorption/ionization in SALDI-IMS. The AuNP-oriented peaks at m/z 196.96 (Au^+) and 393.92 (Au_2^+) were observed in the mass spectrum (80−500 Da) using AuNPs as a matrix which might have caused the suppression of LMWM signals in the mass spectrum. However, higher number molecular signals were obtained without any NP-related peaks using TiO_2 NPs for analysis of mouse brain tissue.

Comparison of Nano-PALDI-IMS with other Imaging Studies. Finally, we illustrated the progress of imaging methods for analysis of biomolecules in tissue samples as compared to Nano-PALDI-IMS analysis. Northen et al. exploited the clathrate nanostructure surface for the identification and imaging of various types of small molecules in mass spectrometry for sensitive detection of molecules from the sample in NIMS.[15] However, the procedure used for sample preparation was found to be tedious, requiring multisteps and was expensive as compared to Nano-PALDI-IMS analysis. Recently, Benabdellah et al. developed a method called "chemical mass spectrometry imaging" to determine the localization of 13 primary metabolites in rat brain using MALDI-IMS, in addition to a few matrix oriented peaks in the mass spectrum.[26] More recently, Shrestha et al. reported the direct analysis of LMWM in mouse brain using atmospheric pressure-infrared matrix-assisted laser desorption ionization (AP-IR-MALDI) and laser ablation electrospray ionization-mass spectrometry (LAESI-MS) for the detection of 40 metabolites with lack of imaging data.[27] In addition, Nemes et al. demonstrated the simultaneous imaging of 200 small metabolites and lipids in rat brain using LAESI-MS where half of the molecules were found to be lipid molecules.[28] The use of secondary ion mass spectrometry (SIMS) for imaging of low molecular weight biomolecules in tissue samples was established for higher spatial resolution (a few 100 nm).[29] The fragmentation of polar headgroup was reported in SIMS as well as the inability to perform MS/MS analyses to confirm the molecules.[30] We also compared our results with the sublimation method for depositing matrix on the surface of brain tissue for imaging of phospholipids in mouse brain where the number of detected signals were found to be less compared to the signals obtained by the proposed method.[31] Shroff et al. investigated the use of 1,8-bis(dimethyl-amino) naphthalene (DMAN; proton sponge), as a novel matrix for MALDI-MS analysis of anions in negative ion mode. The potential of ionless matrixes was target for profiling plant leaf with a 108 monoisotpic peaks in the mass spectrum.[32] On the other hand, in this investigation, TiO_2 NPs were synthesized in a simple and single step approach and were directly used for imaging studies for simultaneously imaging of LMWM (<500 Da).

■ CONCLUSIONS

We believe that the use of TiO_2 NPs in Nano-PALDI-IMS exhibits advantages of simple sample preparation, matrix free background, and detection of a higher number of LMWM signals from the tissue sample. The potentiality of TiO_2 NPs is compared with DHB and gold NPs for imaging of LMWM in tissue samples, and the use of TiO_2 NPs is found to be better in sensitivity and detecting a higher number of biomolecule signals as compared to conventional DHB and gold NPs as matrixes. Finally, the present approach is also demonstrated as a simple, rapid, and inexpensive method for imaging of LMWM in tissue sample as compared to other existing methods such as LDI-MS, NIMS, and LAESI-MS. Nano-PALDI-IMS using TiO_2 NPs can be a useful tool in elucidating the novel findings pertaining to biomarkers of the diseases in biological tissue samples.

■ ASSOCIATED CONTENT

Supporting Information. Additional information as noted in text. This material is available free of charge via the Internet at http://pubs.acs.org.

AUTHOR INFORMATION

Corresponding Author
*Tel/Fax: +81-53-435-2292. E-mail: setou@hama-med.ac.jp.

ACKNOWLEDGMENT

We would like to thank the Japanese society for the Promotion of Science, Japan, for a postdoctoral fellowship (to K.S.). This work was also supported by a Grant-in-Aid for SENTAN from the Japan Science and Technology Agency (to M.S.). CE-MS analysis was supported by a grant for leading metabolome research 2010 provided by Human Metabolomics Technology (http://humanmetabolome.com/) to Y.S.

REFERENCES

(1) Sugiura, Y.; Konishi, Y.; Zaima, N.; Kajihara, S.; Nakanishi, H.; Taguchi, R.; Setou, M. *J. Lipid Res.* **2009**, *50*, 1776–1788.
(2) Weissleder, R.; Pittet, M. J. *Nature* **2008**, *452*, 580–589.
(3) Blow, N. *Nat. Methods* **2008**, *5*, 981–987.
(4) Jansen, J. F.; Backes, W. H.; Nicolay, K.; Kooi, M. E. *Radiology* **2006**, *240*, 318–332.
(5) Bourcier, S.; Benoist, J. F.; Clerc, F.; Rigal, O.; Taghi, M.; Hoppilliard, Y. *Rapid Commun. Mass Spectrom.* **2006**, *20*, 1405–1421.
(6) Petyuk, V. A.; Qian, W. J.; Smith, R. D.; Smith, D. J. *Methods* **2010**, *50*, 77–84.
(7) Karas, M.; Hillenkamp, F. *Anal. Chem.* **1988**, *60*, 2299–2301.
(8) Tanaka, M.; Waki, H.; Ido, Y.; Akita, S.; Yoshida, T. *Rapid Commun. Mass Spectrom.* **1988**, *2*, 151–153.
(9) Sunner, J.; Dratz, E.; Chen, Y. C. *Anal. Chem.* **1995**, *67*, 4335–4342.
(10) Wei, J.; Buriak, J. M.; Siuzdak, G. *Nature* **1993**, *399*, 243–246.
(11) Lee, K. H.; Chiang, C. K.; Lin, Z. H.; Chang, H. T. *Rapid Commun. Mass Spectrom.* **2007**, *21*, 2023–2030.
(12) Watanabe, T.; Okumura, K.; Kawasaki, H.; Arakawa, R. *J. Mass. Spectrom.* **2009**, *44*, 1443–1451.
(13) Chiang, C. K.; Chiang, N. C.; Lin, Z. H.; Lan, G. Y.; Lin, Y. W.; Chang, H. T. *J. Am. Soc. Mass Spectrom.* **2010**, *21*, 1204–1207.
(14) Su, C. L.; Tseng, W. L. *Anal. Chem.* **2007**, *79*, 1626–1633.
(15) Northen, T. R.; Yanes, O.; Northen, M. T.; Marrinucci, D.; Uritboonthai, W.; Apon, J.; Golledge, S. L.; Nordstrom, A.; Siuzdak, G. *Nature* **2007**, *449*, 1033–1036.
(16) Cha, S.; Yeung, E. S. *Anal. Chem.* **2007**, *79*, 2373–2385.
(17) Vidova, V.; Novak, P.; Strohalm, M.; Pol, J.; Havlicek, V.; Volny, M. *Anal. Chem.* **2010**, *82*, 4994–4997.
(18) Taira, S.; Sugiura, Y.; Moritake, S.; Shimma, S.; Ichiyanagi, Y.; Setou, M. *Anal. Chem.* **2008**, *80*, 4761–4766.
(19) Hayasaka, T.; Goto-Inoue, N.; Zaima, N.; Shrivas, K.; Kashiwagi, Y.; Yamamoto, M.; Nakamoto, M.; Setou, M. *J. Am. Soc. Mass Spectrom.* **2010**, *21*, 1446–1454.
(20) Goto-Inoue, N.; Hayasaka, T.; Zaima, N.; Kashiwagi, Y.; Yamamoto, M.; Nakamoto, M.; Setou, M. *J. Am. Soc. Mass Spectrom.* **2010**, *21*, 1940–1943.
(21) Chen, X.; Mao, S. S. *Chem. Rev.* **2007**, *107*, 2891–2959.
(22) Gholipour, Y.; Giudicessi, S. L.; Nonami, H.; Erra-Balsells, R. *Anal. Chem.* **2010**, *82*, 5518–5526.
(23) Sugiura, Y.; Taguchi, R.; Setou, M. *PLoS One* **2011**, *6*, e117952.
(24) Lorkiewicz, P.; Yappert, M. C. *Anal. Chem.* **2009**, *81*, 6596–6603.
(25) Garden, R. W.; Sweedler, J. V. *Anal. Chem.* **2000**, *72*, 30–36.
(26) Benabdellah, F.; Touboul, D.; Brunelle, A.; Laprevote, O. *Anal. Chem.* **2009**, *81*, 5557–5560.
(27) Shrestha, B.; Nemes, P.; Nazarian, J.; Hathout, Y.; Hoffman, E. P.; Vertes, A. *Analyst* **2010**, *135*, 751–875.
(28) Nemes, P.; Woods, A. S.; Vertes, A. *Anal. Chem.* **2010**, *82*, 982–988.
(29) Altelaar, A. F.; Klinkert, I.; Jalink, K.; de Lange, R. P.; Adan, R. A.; Heeren, R. M.; Piersma, S. R. *Anal. Chem.* **2006**, *78*, 734–742.
(30) Yang, H. J.; Sugiura, Y.; Ishizaki, I.; Sanada, N.; Ikegami, K.; Zaima, N.; Shrivas, K.; Setou, M. *Surf. Interface Anal.* **2010**, *42*, 1606–1611.
(31) Hankin, J. A.; Barkley, R. M.; Murphy, R. C. *J. Am. Soc. Mass Spectrom.* **2007**, *18*, 1646–1652.
(32) Shroff, R.; Rulísek, L.; Doubsky, J.; Svatos, A. *Proc. Natl. Acad. Sci.* **2009**, *106*, 10092–10096.

Experimental and Molecular Pathology 91 (2011) 614–621

Contents lists available at ScienceDirect

Experimental and Molecular Pathology

journal homepage: www.elsevier.com/locate/yexmp

Imaging mass spectrometry analysis reveals an altered lipid distribution pattern in the tubular areas of hyper-IgA murine kidneys

Yukihiro Kaneko [a,*], Yoko Obata [b], Tomoya Nishino [b], Hiroshi Kakeya [b], Yoshitsugu Miyazaki [a], Takahiro Hayasaka [c], Mitsutoshi Setou [c], Akira Furusu [b], Shigeru Kohno [b]

[a] Department of Chemotherapy and Mycoses, National Institute of Infectious Disease, Toyama 1-23-1, Shinjuku-ku, Tokyo 162-8640, Japan
[b] Department of Molecular Microbiology and Immunology, Nagasaki University Graduate School of Biomedical Sciences, 1-7-1 Sakamoto, Nagasaki 852-8501, Japan
[c] Department of Cell Biology and Anatomy, Hamamatsu University School of Medicine, 1-20-1 Handayama, Higashi-ku, Hamamatsu, Shizuoka 431-3192, Japan

ARTICLE INFO

Article history:
Received 7 July 2011
Available online 23 July 2011

Keywords:
Imaging mass spectrometry
Phosphatidylcholine
Urine
Lipid
IgA
Nephropathy
Urinary stagnation
Molecular distribution
Molecular imaging
Deposition

ABSTRACT

Immunoglobulin A (IgA) nephropathy is the most common glomerular disease worldwide. To investigate the pathogenesis of this renal disease, we used animal models that spontaneously develop mesangioproliferative lesions with IgA deposition, which closely resemble the disease in humans. We analyzed the molecular distribution of lipids in hyper-IgA (HIGA) murine kidneys using matrix-assisted laser desorption/ionization-quadrupole ion trap-time of flight (MALDI-QIT-TOF)-based imaging mass spectrometry (IMS), which supplies both spatial distribution of the detected molecules and allows identification of their structures by their molecular mass signature. For both HIGA and control (Balb/c) mice, we found two phosphatidylcholines, PC(16:0/22:6) and PC(18:2/22:6), primarily located in the cortex area and two triacylglycerols, TAG(16:0/18:2/18:1) and TAG(18:1/18:2/18:1), primarily located in the hilum area. However, several other molecules were specifically seen in the HIGA kidneys, particularly in the tubular areas. Two HIGA-specific molecules were O-phosphatidylcholines, PC(O-16:0/22:6) and PC(O-18:1/22:6). Interestingly, common phosphatidylcholines and these HIGA-specific ones possess 22:6 lipid side chains, suggesting that these molecules have a novel, unidentified renal function. Although the primary structure of the HIGA-specific molecules corresponding to *m/z* 854.6, 856.6, 880.6, and 882.6 remained undetermined, they shared similar fragmentation patterns, indicating their relatedness. We also showed that all the HIGA-specific molecules were derived from urine, and that artificial urinary stagnation—due to unilateral urethral obstruction—caused HIGA-specific distribution of lipids in the tubular area.

Introduction

Histopathological findings have provided a significant amount of information on nephropathies and have been used to solve their underlying mechanisms, such as IgA deposition in IgA nephropathy (Muda et al., 1995). In recent years, the emergence of molecular imaging techniques such as green fluorescent protein labeling and immunohistochemistry have expanded the practical applications available to researchers (Drummond and Allen, 2008; Grunkin et al., 2011). Although the techniques for histopathology have been useful in investigating the morphology and distribution of various defects in tissues, conventional techniques such as electron microscopy have failed to identify low-molecular-weight compounds. Moreover, while new systematic approaches (e.g., proteomics and metabolomics using mass spectrometry (MS)) have enabled the identification of various kinds of molecular species and have contributed to a more detailed understanding of the etiology of the disease, as well the discovery of new biomarkers (Baronas et al., 2007; Mimura et al., 1996; Yasuda et al., 2006; Yoshioka et al., 2009; Zhang et al., 2008), these approaches lose the distributional information.

Matrix-assisted laser desorption/ionization-quadrupole ion trap-time of flight (MALDI-QIT-TOF)-based imaging mass spectrometry (IMS) is a technique that supplies both the spatial distribution of the detected molecules and allows the identification of their structures by their molecular mass signature. More recently, the resolution of MALDI-QIT-TOF-IMS has been refined to microscopic level, thereby enabling an analysis of microscopic lesions that conventional approaches have not been able to easily examine (Setou and Kurabe, 2011). Willems et al. recently reported the usefulness of the IMS technology for grading myxoid sarcoma by clustering of the biomolecular signatures in particular lipid compositions (Willems et al., 2010).

The relationship between lipid composition and kidney diseases is not well understood. Hence, we investigated the distribution of lipid compositions in the kidneys of HIGA mice—well-recognized murine

* Corresponding author at. Fax: +81 3 5285 1272.
E-mail address: ykaneko@nih.go.jp (Y. Kaneko).

0014-4800/$ – see front matter © 2011 Elsevier Inc. All rights reserved.
doi:10.1016/j.yexmp.2011.07.002

model for IgA nephropathy (Muso et al., 1996)—using MALDI-QIT-TOF-IMS and analyzed the physiological significance of the molecules detected by it.

Materials and methods

Chemicals

All general chemicals used in this study were purchased from Wako Chemicals (Tokyo, Japan), unless otherwise indicated, and were of the highest purity available. Ultra pure water dispensed by a Milli-Q water system (Millipore, Bedford, MA, USA) was used for the preparation of buffers and solvents.

Animals and sample preparation

All the experiments on the mice were conducted according to the protocols approved by the Animal Care and Use Committee, Nagasaki University, School of Medicine. Kidneys were obtained from 28-week-old Balb/c mice and HIGA mice (Charles River Japan, Kanagawa, Japan), and urine was collected in a cage designed to prevent feces–urine contact (Nalge Nunc International, Tokyo, Japan), as previously described (Kurashige et al., 2008). The tissue samples and urine were immediately frozen and stored at −80 °C until use.

Tissue slice preparation

Tissue slice preparation for imaging mass spectrometry was performed as previously described (Hayasaka et al., 2008; Sugiura and Setou, 2009). Briefly, the frozen intact tissues were sectioned at −20 °C in a cryomicrotome (CM 3050; Leica Microsystems, Wetzlar, Germany) to obtain 5-μm-thick sections, and the frozen slices were then thaw-mounted on indium tin oxide (ITO)-coated glass slides (Bruker Daltonics, Leipzig, Germany). Matrix was coated on the slices by spraying them with 100 μl of 2,5-dihydroxybenzoic acid (Bruker Daltonics) solution (50 mg/ml in 70% methanol/0.1% trifluoroacetic acid) using a 0.2-mm nozzle caliber airbrush (Procon Boy FWA Platinum; Mr. Hobby, Tokyo, Japan). After drying, the ITO slide was adhered to a mass spectrometer target plate with double-sided conductive adhesive tape to facilitate electrical conduction. Positional information for each section was obtained by scanning the section with a chemical inkjet printer CHIP-1000 (Shimadzu Corporation, Kyoto, Japan) prior to MALDI-QIT-TOF-MS analysis.

Extraction of lipids from tissue and urine

Tissues were crudely ground using clean spatulas and further shredded using a sonicator in an approximately 20-fold volume of chloroform-methanol (2:1) in glass tubes on ice. The mixture was

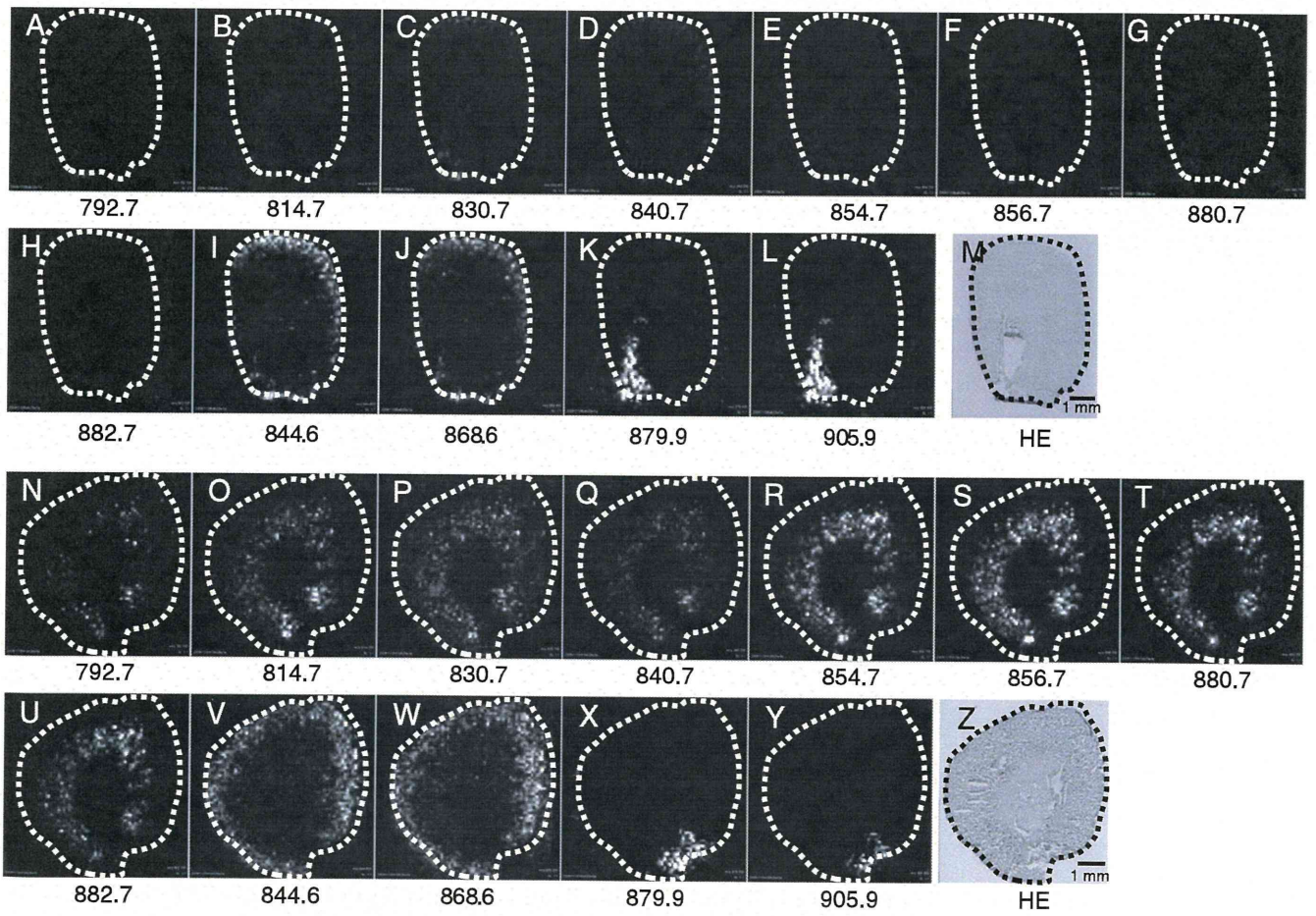

Fig. 1. Eight mass peaks are dominant in the kidneys of HIGA mouse in mass images of kidneys. Significant peaks, *m/z* 792.6, *m/z* 814.6, *m/z* 830.6, *m/z* 840.6, *m/z* 854.6, *m/z* 856.6, *m/z* 880.6, and *m/z* 882.6, are detected in HIGA kidneys (N–U), but absent in the control (A–H). However, 2 significant mass peaks are seen in the peripheral (cortex) area (I,J,V,W), and 2 other significant mass peaks are seen in the hilum area (K,L,W,Y) in both HIGA and control kidneys. The corresponding HE images of the control (M) and HIGA (Z) are also shown. Scale bars indicate a length of 1 mm.

centrifuged at 3000 rpm for 5 min at 4 °C. The supernatant was collected and evaporated, and the dried sample was used for further extraction by the Bligh and Dyer (BD) method (Bligh and Dyer, 1959). Briefly, to 1 ml of the original volume of supernatant, 0.08 ml of water and 0.3 ml of chloroform/methanol (1:2) were added and mixed. Next, 0.1 ml of chloroform was added and mixed, followed by the adding and mixing of 0.1 ml of water. The suspension was then centrifuged at 3000 rpm for 5 min at 4 °C. The organic phase was collected and evaporated, and then reconstituted in appropriate volume of methanol.

Extraction from urine was also performed by the BD method. Briefly, 0.3 ml of chloroform/methanol (1:2) was added to 0.08 ml of urine, and the extraction was performed as above.

These extracted samples were then used for MALDI-QIT-TOF-MS or liquid chromatography-linear ion trap quadrupole-Orbitrap-MS (LC-LTQ-Orbitrap-MS).

Unilateral urethral obstruction

For allowing urine to stagnate, 28-week-old Balb/c mice received unilateral urethral obstruction (UUO), as previously described (Li et al., 2010). Briefly, the left mid-ureter was obstructed by two-point ligations with silk sutures. The mice were sacrificed 2 weeks later.

MALDI-QIT-TOF-MS

All analyses were performed in positive ion mode and in mid-mass range by using a MALDI-QIT-TOF-type mass spectrometer (AXIMA-QIT; Shimadzu Corporation and Kratos Analytical, Manchester, UK), equipped with a 337 nm nitrogen laser, as previously described (Hayasaka et al., 2008; Sugiura and Setou, 2009). An external calibration method was performed with ions from angiotensin II and its decomposition products covering from *m/z* 680 to 900.

Data acquisition and imaging

The data acquisition and processing were controlled by Launchpad software (Kratos Analytical). All the spectra were recorded with the standard instrument settings for optimum transmission. Each raster scan was performed in square regions of 5000 μm to 8000 μm with a measurement pitch of 100 μm automatically. Laser irradiation consisted of 10 shots in each spot, and the power setting was 50 to 60 as appropriate. The raw data were converted by using free software (Axima2Analyze; Novartis, Basel, Switzerland), to apply the BioMap (Novartis). Mass signals between *m/z* 600 and *m/z* 1000 were analyzed with an interval of 0.1 and a tolerance of 0.05, resulting in 4001 images for each experiment. The ion image highlighted the signal intensity obtained from a specific molecule.

Tandem MS analysis

The instrument settings were changed to correspond to the ions from the molecules of interest. The power and collision-induced dissociation (CID) settings were adjusted from 50 to 60 and from 200 to 400, respectively.

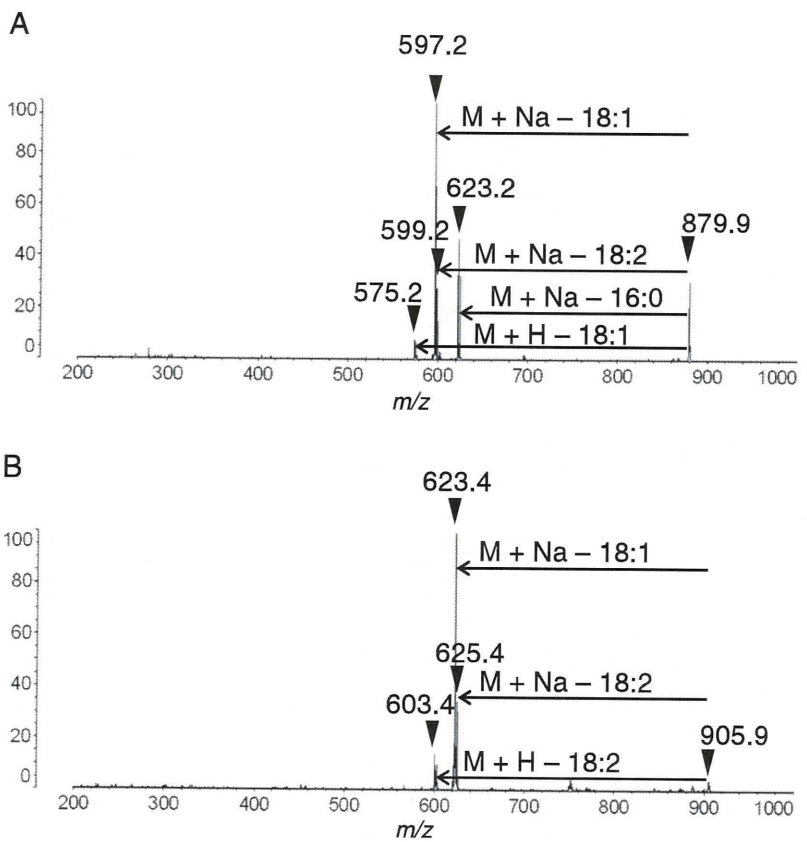

Fig. 2. Two triacylglycerols are present in the renal hilum. The fragmentation patterns of the molecules *m/z* 879.9 (A) and *m/z* 905.9 (B) in tandem MS analysis were involved with the loss of fatty acids and thereby identified as the triacylglycerols [TAG 16:0/18:2/18:1 + Na] + (A) and [TAG 18:1/18:2/18:1 + Na] + (B), respectively.

MS analysis of extracted lipids from kidney homogenates or urine

Approximately, 5 to 10 μl of lipid extracts were dried on ITO slides and coated by spraying the matrix solution. For inferring the adduct ion, 10 mM (final concentration) sodium or potassium acetate was added to extracted samples since excessive sodium or potassium ions have been shown to modify the signal intensity of polar lipids (Sugiura and Setou, 2009). The procedure was performed, as described above.

LC-LTQ-Orbitrap-MS

LC-LTQ-Orbitrap-MS analysis using an Agilent 1200 system was performed to determine the primary structures of the molecules. All procedures were performed in Kazusa DNA Research Institute, Kisarazu, using a detailed protocol, described previously (Iijima et al., 2008). Briefly, the extracted sample reconstituted in methanol was applied to a TSK-GEL Octyl-80Ts (TOSOH Corporation, Tokyo, Japan). Water (solvent A) and acetonitrile (solvent B) were used as the mobile phase with 0.1% v/v formic acid added to both solvents. The gradient program was as follows: 80% B (0 min), 90% B (20 min), 95% B (40 min), 97% B (60 min), 98% B (80 min), 99% B (100 min), 99% B (110 min), 80% B (110.1 min), and 80% B (120 min). The flow rate was set to 0.015 ml/min, and the column oven temperature at 40 °C; 20 μl of each sample was injected.

Data were analyzed with a molecular formula calculation by using the following databases: KEGG (http://www.genome.jp/kegg/), KNApSAcK (http://kanaya.naist.jp/KNApSAcK/), Flavonoid Viewer (http://www.metabolome.jp/software/FlavonoidViewer/), and LIPID MAPS (http://www.lipidmaps.org/). Molecular species were confirmed by tandem MS of selected peaks and by collating each peak's accurate mass measurement with those from the databases.

Results

Molecular distribution of lipids in the HIGA kidney differs from that in the control kidney

Eight mass peaks—*m/z* 792.6, *m/z* 814.6, *m/z* 830.6, *m/z* 840.6, *m/z* 854.6, *m/z* 856.6, *m/z* 880.6, and *m/z* 882.6—were strongly represented in the HIGA kidney (Figs. 1N–U), but not in the control (Figs. 1A–H). However, 2 significant mass peaks, *m/z* 844.6 and *m/z* 868.6, in the peripheral (cortex) area (Figs. 1I, J, V, W) and 2 significant mass peaks, *m/z* 879.9 and *m/z* 905.9, in the hilum area (Figs. 1K, L, X, Y) were observed in both the HIGA and control kidneys.

Two triacylglycerols identified in the hilum

Tandem MS analysis revealed that the fragmentation patterns of the molecules *m/z* 879.9 and *m/z* 905.9 were involved in the loss of fatty acids and were identified as the triacylglycerols (TAGs) [TAG (16:0/18:2/18:1) + Na] + and [TAG(18:1/18:2/18:1) + Na]+, respectively, by collating them with existing TAGs in the database (Fig. 2).

Several lipids in the cortex are phosphatidylcholines

LC-LTQ-Orbitrap-MS analysis showed that *m/z* 806.57 and *m/z* 830.57 were commonly seen in lipids extracted from Balb/c and HIGA kidneys (Figs. S1A, B). Tandem MS identified these peaks to correspond to [PC(16:0/22:6) + H] + and [PC(18:2/22:6) + H]+, respectively (Figs. S1C, D). In addition, *m/z* 844.6 and *m/z* 868.6 were estimated to be carrying a potassium ion as the adduct ion (Fig. 3), and thus, were considered to correspond to [PC(16:0/22:6) + K] + and [PC (18:2/22:6) + K]+, respectively.

HIGA-specific lipids in the tubular lesions are O-phosphatidylcholines that are possibly related to phosphatidylcholines in the cortex area

LC-LTQ-Orbitrap-MS also revealed that *m/z* 792.59 and *m/z* 818.61 were seen specifically in HIGA (Fig. S1B), and tandem MS analysis determined that they corresponded to [PC(O-16:0/22:6) + H] + and [PC(O-18:1/22:6) + H]+, respectively (Figs. S1E, F). In addition, *m/z* 814.6 and *m/z* 840.6 were estimated to be carrying a sodium ion as an adduct ion, while *m/z* 830.6 was estimated to be carrying a potassium ion (Fig. 3). Accordingly, *m/z* 792.6, *m/z* 814.6, *m/z* 830.6, and *m/z* 840.6 were considered to correspond to [PC(O-16:0/22:6) + H]+, [PC(O-16:0/22:6) + Na]+, [PC(O-16:0/22:6) + K]+, and [PC (O-18:1/22:6) + Na]+, respectively.

LC-LTQ-Orbitrap-MS failed to identify the corresponding molecules of *m/z* 854.6, *m/z* 856.6, *m/z* 880.6, and *m/z* 882.6 because the mass peaks compatible to them were absent; however, the adduct ion of these molecules were speculated to be a sodium ion (Fig. 3). Moreover, the fragmentation patterns analyzed by on-section tandem MS analysis revealed that these molecules possessed a regularity of arrangement and were part of orderly structures (Fig. 4).

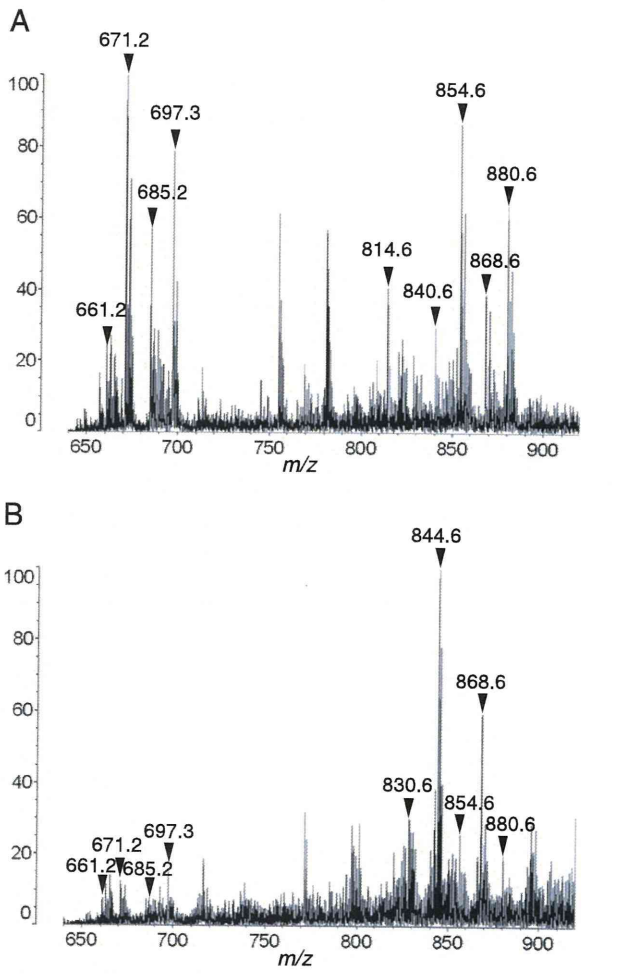

Fig. 3. Addition of sodium or potassium ions in the lipid extracts implied the identity of the adduct ions. The mass peak signals *m/z* 814.6, *m/z* 840.6, *m/z* 854.6, *m/z* 856.6, *m/z* 880.6, and *m/z* 882.6 are intensified when sodium ions are added in the lipid extracts of HIGA kidneys (A); *m/z* 830.6, *m/z* 844.6, and *m/z* 868.6 are intensified when potassium ions are added (B); but *m/z* 792.6 was not intensified in either condition. Thus, these results imply that the adduct ion of *m/z* 814.6, *m/z* 840.6, *m/z* 854.6, *m/z* 856.6, *m/z* 880.6, and *m/z* 882.6 might be sodium, and the adduct ion of *m/z* 830.6, *m/z* 844.6, and *m/z* 868.6 might be potassium.

Urinary stagnation causes HIGA-specific distribution of lipids in the tubular area

For understanding the source from where HIGA-specific molecules were derived, it was important to investigate whether these lipids were excreted in urine. Mass peaks of lipids extracted from urine were investigated using MALDI-QIT-TOF-MS and compared with those from the kidney. The results showed that significant mass peaks in the urine matched the HIGA-specific mass peaks in the kidney (Fig. 5). Thus, we verified that the HIGA-specific molecules were lipids that were normally excreted in urine. We also found that the artificial urinary stagnation due to UUO in Balb/c mice could reproduce the HIGA-specific distribution of lipids in the tubular area (Fig. 6) and that these molecules were, therefore, derived from the urine.

Discussion

We revealed the molecular distribution of lipids in the kidneys, hypothesized on the underlying mechanisms causing the HIGA-specificity, and determined the identity of several molecules by using IMS in combination with LC-LTQ-Orbitrap-MS (Table 1).

We noticed a similarity among PC(16:0/22:6), PC(18:2/22:6), PC(O-16:0/22:6), and PC(O-18:1/22:6) (Fig. 7). All these molecules have 22:6 lipid side chains. Molecules that were common in both the HIGA and normal kidneys were regular PCs and were distributed in the cortex area; while HIGA-specific molecules were O-PCs and distributed in the tubular areas. In addition, the only difference between PC(16:0/22:6) and PC(O-16:0/22:6) was an oxygen atom in the 16:0 side chains. Similarly, the only differences between PC(18:2/22:6) and PC(O-18:1/22:6) were an

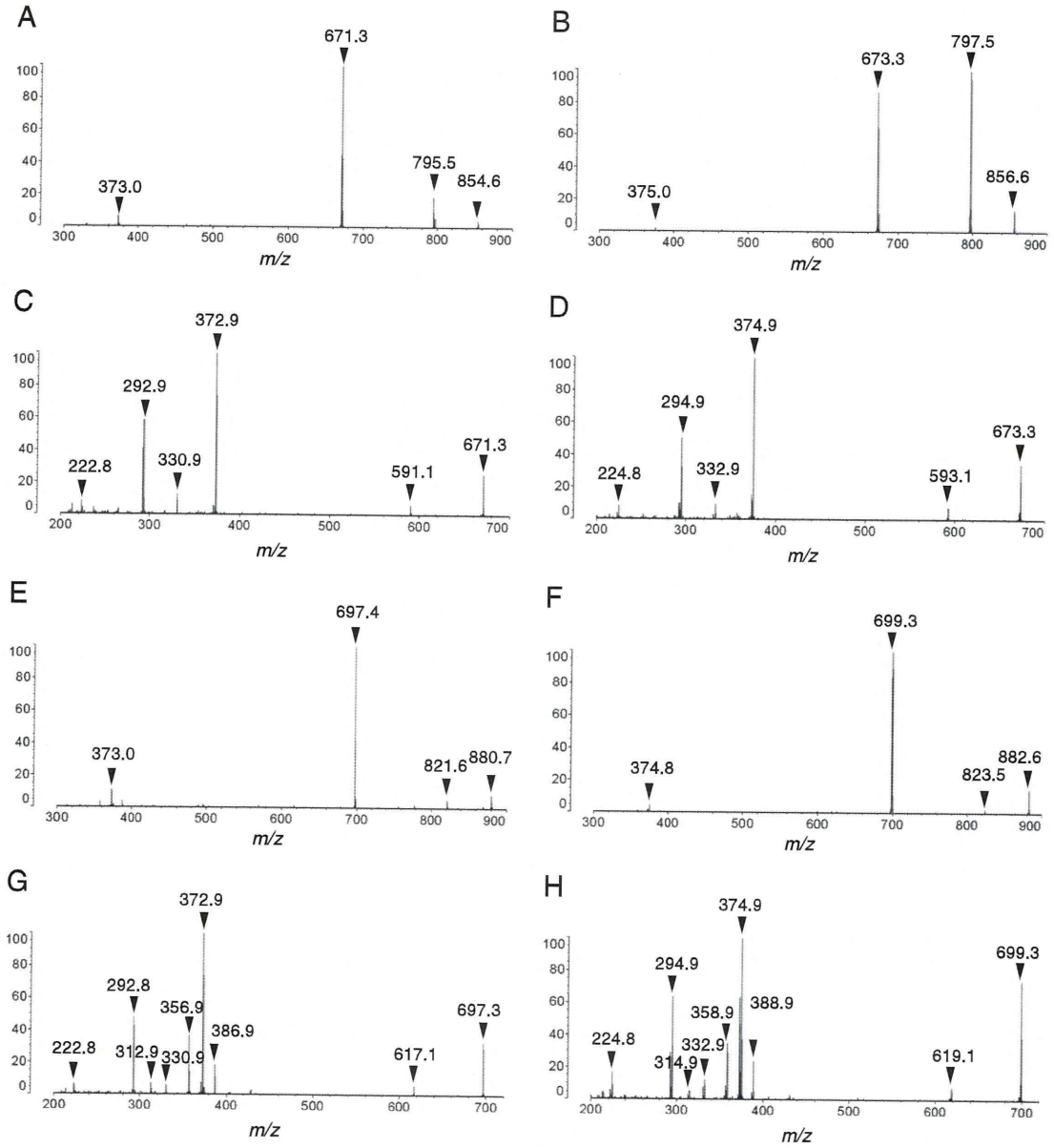

Fig. 4. Tandem MS analysis of HIGA kidney-specific mass peaks *m/z* 854.6, *m/z* 856.6, *m/z* 880.6, and *m/z* 882.6 shows their molecular relationship. The fragmentation patterns of the molecules of *m/z* 854.6, *m/z* 856.6, *m/z* 880.6, and *m/z* 882.6 by MS-MS analysis are involved with the loss of *m/z* 59 Da and *m/z* 183 Da (A,B,E,F). Subsequent MS3 analysis failed to identify these molecules, but the similarity in their fragmentation patterns suggests that they are related molecules (C,D,G,H).